Nuclear medium effects in lepton-nucleus DIS in the region of $x \gtrsim 1$

M. Sajjad Athar, S. K. Singh, and F. Zaidi*

Department of Physics, Aligarh Muslim University, Aligarh - 202002, India

(Received 11 February 2022; accepted 19 April 2022; published 6 May 2022)

The nuclear medium effects in the nuclear structure functions and differential cross sections in the deep inelastic scattering (DIS) of charged lepton and neutrino from nuclear targets are studied in the region of large x including $x \geq 1$. The nuclear medium effects due to the Fermi motion and the binding energy of nucleons and the nucleon correlations are included using nucleon spectral function calculated in a microscopic field theoretical model. The numerical results for the nuclear structure functions and the cross sections are obtained using the nucleon structure function evaluated at the next-to-next-to-leading order (NNLO) with the Martin-Motylinski-Harland Lang-Thorne (MMHT) parametrization of the nucleonic parton distribution functions (PDFs) and are compared with the available experimental data on electron scattering from the Jefferson Lab (JLab) and SLAC Nuclear Physics Facility (NPAS). In the case of neutrino scattering the results are relevant for understanding the DIS contributions to the recent inclusive cross sections measured by the Main Injector Neutrino Experiment to study ν-A interactions (MINERvA) as well as theoretical predictions are made for Deep Underground Neutrino Experiment (DUNE). The importance of isoscalarity corrections in heavier nuclear targets as well as the effect of the kinematic cut on the CM energy W in defining the DIS region have also been discussed.

DOI: 10.1103/PhysRevD.105.093002

I. INTRODUCTION

The experimental evidence of the nuclear medium effects in the deep inelastic scattering (DIS) of the charged leptons from the heavier nuclear targets was first reported by the European Muon Collaboration (EMC) when it measured the cross sections for $\mu^- - {}^{56}\mathrm{Fe}$ and $\mu^- - {}^{2}\mathrm{D}$ scattering processes and found that the ratio of the cross sections per nucleon in ${}^{56}\mathrm{Fe}$ and ${}^{2}\mathrm{D}$ is not unity [1]. As the DIS cross sections are generally expressed in terms of the nucleon structure functions, the EMC observation implied that the structure functions for a nucleon bound inside a nucleus are different from the structure functions of a free nucleon. This was surprising as the underlying degrees of freedom participating in the DIS process are quarks and gluons. This effect is famously known as the EMC effect. Later more experiments confirmed this EMC observation for $(\frac{A}{A'})(\frac{\sigma_{A'}}{\sigma_A})$, where A and A' are the nucleon number for the different nuclear targets [2–8]. The deviation of the ratio $(\frac{A}{A'})(\frac{\sigma_{A'}}{\sigma_A})$ from unity underlines the importance of the nuclear medium effects through the structure of the EMC effect and is categorized in four broad categories depending upon the different regions of x, for example, the shadowing and antishadowing effects in the region of $0 < x < 0.1$ and $0.1 < x < 0.2$, the EMC effect in the region of $0.2 < x < 0.7$ and the Fermi motion effect in the region of $x \geq 0.7$. For the free nucleon target, the Bjorken variable x lies in the region of $0 \leq x \leq 1$ while for a nuclear target it can vary from 0 to A, i.e., $0 \leq x \leq A$. To explore the region of $x > 1$ lepton induced deep inelastic scattering from a nuclear target is the conventional method and the quarks carrying momentum fraction greater than the momentum of nucleon at rest are referred as the "superfast quarks" in the literature. These superfast quarks may be described via understanding the different properties of quantum chromodynamics (QCD) like the behavior of nuclear forces at very short distances and the nuclear medium modifications of parton distributions in nuclei. Several nuclear PDFs parametrizations are available in the literature and continuously being updated [9–15]. In the region of x larger than 1, i.e., $x \geq 1$ (inaccessible for the free nucleons), some experimental efforts have been made to study the charged lepton-nucleus inclusive scattering processes [16–22], while in the weak sector, not many studies have been made to explore the region of $x \geq 1$ [23,24].

The neutrino-nucleus scattering experiment MINERvA at the Fermilab [23,25] has been performed to make EMC kind of measurements using medium and heavy nuclear targets like hydrocarbon, water, iron and lead in a wide range of x and Q^2. This experiment is not only giving the

*Corresponding author.
zaidi.physics@gmail.com

information on the hadron dynamics in the nuclear medium for weak interaction induced processes in the wide region of x and Q^2 but it would also be helpful in understanding the nuclear model dependence of $\nu_l(\bar{\nu}_l) - A$ scattering cross section. This is important for interpretation of the neutrino oscillation experiments being done using nuclear targets. A better understanding of scattering cross section is required to reduce the systematics which has presently 25–30% contribution due to the lack in the understanding of neutrino-nucleus scattering cross sections. In the first results from MINERvA collaboration, Tice *et al.* [23] have reported the experimental results for the ratios of differential cross section, i.e., $(\frac{d\sigma_A/dx}{d\sigma_{\rm CH}/dx})$; $(A = {}^{12}{\rm C}, {}^{56}{\rm Fe}, {}^{208}{\rm Pb})$ for the $\nu_\mu - A$ inclusive scattering processes using the low energy neutrino beam (peaks around neutrino energy $E_{\nu_l} = 3$ GeV) in the energy region of $2 \leq E_{\nu_l} \leq 20$ GeV in a wide range of x, i.e., $x \leq 1.5$. They observed that theoretical as well as phenomenological models proposed to include the nuclear medium effects are not able to explain the MINERvA's experimental data [23] satisfactorily. Later Mousseau *et al.* [25] have reported the neutrino-nucleus deep inelastic scattering data using the medium energy neutrino beam in the energy region of $E_\nu =$ 5–50 GeV with kinematic constrains of $Q^2 \geq 1$ GeV^2 and $W \geq 2$ GeV, and have compared the experimental results with the results of phenomenological models given by Bodek *et al.* [26], Cloet *et al.* [27] as well as with the results obtained from the GENIE Monte Carlo (MC) event generator [28]. They observed that the different phenomenological models [26–28] considered in their analysis [25] are unable to explain the entire region of Bjorken x. In a recent work, Zaidi *et al.* [29] have theoretically studied the $\nu_l(\bar{\nu}_l) - A$ deep inelastic cross sections in carbon, hydrocarbon, iron and lead nuclei using a microscopic field theoretical model which has also been used earlier to study the nuclear medium effects in the charged lepton-nucleus DIS cross sections for several nuclear targets in a wide range of x and Q^2 [30–32]. The numerical results for the ratio $(\frac{d\sigma_A/dx}{d\sigma_{\rm CH}/dx})$; $(A = {}^{12}{\rm C}, {}^{56}{\rm Fe}, {}^{208}{\rm Pb})$ vs x at $E_\nu = 7$ GeV and 25 GeV (Fig. 14 of Ref. [29]) were compared by them [29] with the experimental results from MINERvA collaboration [25] and also with the phenomenological results given by Bodek *et al.* [26], Cloet *et al.* [27] and the GENIE MC generator [28]. It has been concluded that these phenomenological models as well as the theoretical model used by them are not able to satisfactorily explain the ratio in the entire region of Bjorken x. In a recent MINERvA's analyses for ν_μ induced charged current inclusive scattering process off hydrocarbon target, the results for the differential cross sections as a function of lepton kinematics like the longitudinal and transverse momenta of muons have been reported by Ruterbories *et al.* (in Fig. 16) [33] and Filkins *et al.* (in Figs. 13 and 14) [34], where they have compared the results from MINERvA experiment with the results from the theoretical model developed by our group (labeled as AMU DIS) [29,31,35] and also with the phenomenological results of nCTEQ15 [36] and nCTEQnu [37]. They conclude that although the theoretical predictions and the phenomenological results show reasonable agreement among themselves but none of them are able to completely explain the MINERvA's experimental data in the entire range of charged lepton momentum taken into consideration.

Presently, the experimental analysis of the (anti)neutrino induced inclusive scattering data using intermediate energy (anti)neutrino beam in the energy region of 5–50 GeV peaking at the (anti)neutrino energy $E_{\nu_l} = 6$ GeV is under process. This would provide new data in a wide range of x, including the higher region of $x \gtrsim 1$ [38]. Moreover, the current and future experiments at the Fermilab with the short-baseline and long-baseline neutrino beams like ICARUS [39,40], SBND [41,42], MicroBooNE [43] and DUNE [44–46] are also aiming the measurements of neutrino-nucleus scattering cross sections, specifically, using the liquid argon as a nuclear target. The liquid argon scintillators are being used due to their capability of excellent neutrino flavor identification and neutrino energy reconstruction. ICARUS [39,40], SBND [41,42] and MicroBooNE [43] experiments are focused to explore the energy region of a few GeV, however, DUNE experiment [44–46] has a wide energy spectrum which spans up to tens of GeV. Earlier ArgoNeuT experiment [47] was performed at the Fermilab using the NuMI neutrino beamline which first reported the results of the inclusive cross sections for mean neutrino energy $\langle E_{\nu_l} \rangle = 4.3$ GeV in the charged current $\nu_\mu - {}^{40}{\rm Ar}$ scattering process. Later, the measurements were also made for the $\bar{\nu}_\mu$ induced inclusive scattering off argon with a mean antineutrino energy of 3.6 GeV [48].

In the energy region of a few GeV, the contribution to the neutrino-nucleus cross section comes from the quasielastic, resonance production and deep inelastic scattering processes. It is not easy to exactly define the kinematic regions corresponding to these processes but one can classify them depending upon the dominance of a particular process. For example, in the low energy region $E_{\nu_l} < 1$ GeV it is the quasielastic scattering which gives dominant contribution to the cross section and in the energy region of $1 \leq E_{\nu_l} \leq$ 3 GeV the inelastic scattering processes dominate while in the energy region of $E_{\nu_l} > 3$ GeV the DIS dominates. However, there is significant contributions of the higher resonance production in the region of $E_{\nu_l} \geq 3$ GeV, while the contribution of the DIS in the energy region of $E_{\nu_l} \leq$ 3 GeV is also not small. In view of this the kinematic region around $E_{\nu_l} \approx 3$ GeV is designated as the transition region of resonance production and DIS. The sharp kinematic boundaries defining the transition regions are not defined uniquely. Therefore, in the literature to define the DIS region, the kinematic constrain on W has varied

from 1.4 to 2.0 GeV and it has been extrapolated to lower values of $Q^2 < 1$ GeV^2 [49–52]. Due to the ambiguity in the definitions of the transition region, there exists an uncertainty in calculating the total cross sections while summing over the cross section contributions from the resonance production and DIS processes. Hence, it is important to properly define the kinematic boundaries for the transition region. In MINERvA's experimental analysis the region of $Q^2 > 1$ GeV^2 and $W > 2$ GeV is considered to be the region of pure or true DIS [25]. The same kinematic constrains to define the region of pure DIS have been used in the neutrino event generators such as NEUT [53] and GENIE Monte Carlo [28] which is widely used by the neutrino physics community. Moreover, the neutrino-nucleus interactions in the shallow and deep inelastic scattering regions have also been discussed in the NuSTEC workshop held at L'Aquila in 2018 [54] as well as in the Snowmass conference held in 2021 [55]. It has been observed that at the center of mass energy $W > 1.08$ GeV, i.e., above the pion production threshold $\Delta(1232)$ resonance excitation gives dominant contribution to the scattering cross sections, however, as one moves toward the higher W region hadron dynamics results from a nontrivial interplay of overlapping baryon resonances, nonresonant amplitudes and their interference. The region of shallow inelastic scattering is defined as the sum of resonant and nonresonant pion production processes above $\Delta(1232)$ production threshold and at $Q^2 \lesssim 1$ GeV^2 contributing to the inclusive scattering process [56]. The understanding of neutrino physics in these kinematic regions is important in order to interpret the experimental results from the current and future oscillation experiments using accelerator and atmospheric neutrinos. In the review article by Athar *et al.* [57] and also in Ref. [35], the transition region and corresponding kinematical constrains are discussed in detail.

In Fig. 1, we have shown the kinematic region of x and Q^2 covered by the neutrino-nucleus scattering experiments viz. NuTeV [58], CDHSW [59], CCFR [60], and CHORUS [61] and some of the charged lepton-nucleus scattering experiments viz. EMC [1], NMC [3], NE18 [17], E89-008 at JLab [18], CLAS [20], NPAS [21]. One may notice that there is lack of experimental data in the region of $x > 0.8$ for both the electromagnetic as well as weak interaction channels. Therefore, more experimental measurements are required to explore the nucleonic properties and the lepton production cross section in this kinematic region. In this figure, we have also shown the corresponding kinematic regions in the $x - Q^2$ plane for the free nucleon target (right panel) at the two different values of incoming lepton energies (either neutrino or charged lepton) viz. $E_l = 3$ GeV and $E_l = 7$ GeV with outgoing lepton energies

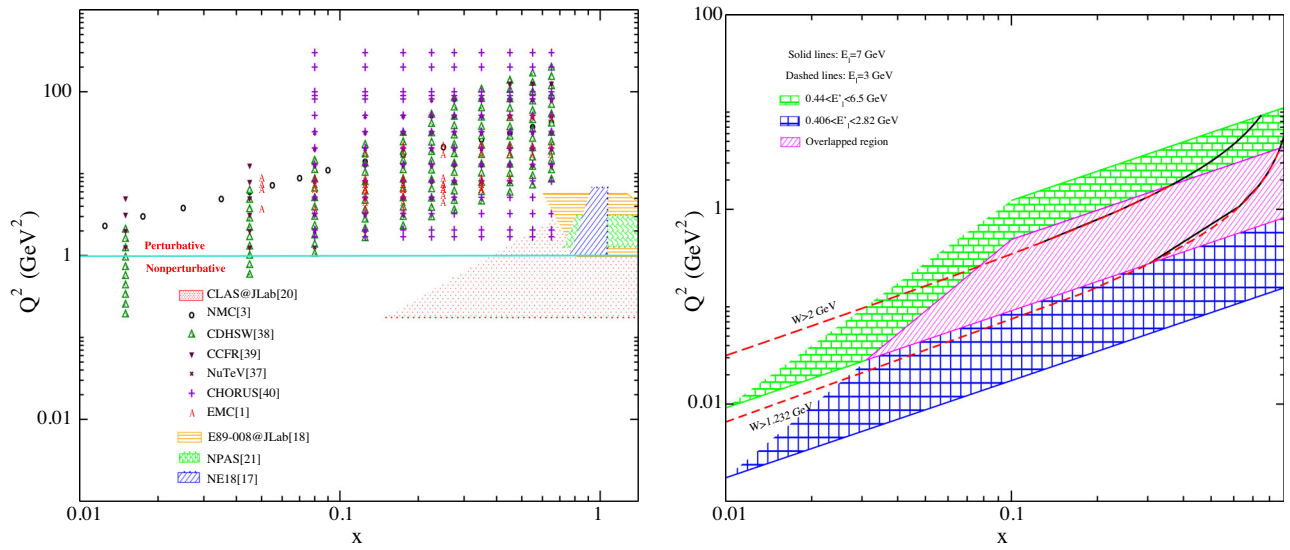

FIG. 1. Left panel: kinematic region in $x - Q^2$ plane, where most of the experimental data are available from charged lepton-nucleus [1,3,17,18,20,21] and neutrino-nucleus [58–61] scattering off various nuclei like ^{12}C, ^{56}Fe and ^{208}Pb. The data from CLAS (red dotted pattern), NE18 (blue diagonal lines pattern), E89-008 (orange horizontal lines pattern) and NPAS (green down wave pattern) experiments are shown by the band. Right panel: the two bands in the figure show the kinematic region of outgoing charged lepton energy (E_l') in the range of $0.406 < E_l' < 2.82$ GeV (square pattern) and $0.44 < E_l' < 6.5$ GeV (brick pattern) corresponding to the incoming beam energies viz. $E_l = 3$ GeV and $E_l = 7$ GeV, respectively. The overlapped region of these energies is shown by the band filled with diagonal lines. The dashed (solid) lines show the $x - Q^2$ region for $E_l = 3(7)$ GeV when a cut on the CM energy viz. $W > 1.232$ GeV and $W > 2$ GeV is applied. The kinematic region of $x > 1$ which is inaccessible for the free nucleon target (right panel) may be explored using a nuclear target (left panel) as shown in the present figure. Therefore, the investigation of deep inelastic scattering in the kinematic region $x > 1$ has significant importance in the understanding of nuclear medium effects.

E_l' lying in the range of $0.406 \le E_l' \le 2.82$ GeV and $0.44 \le E_l' \le 6.5$ GeV, respectively. The effect of the center of mass energy cuts of $W > 1.2$ GeV and $W > 2$ GeV has also been shown on the allowed kinematic region in the $x - Q^2$ plane as these quantities are related as:

$$x = \frac{Q^2}{2M_N(E_l - E_l')}, \qquad Q^2 = -q^2 \ge 0,$$
$$W^2 = M_N^2 + Q^2\left(\frac{1}{x} - 1\right) \tag{1}$$

with M_N as the target nucleon mass.

In the considered kinematic region of high x and moderate Q^2 the nonperturbative effects like the target mass corrections (TMC) and higher twist corrections (HT) that involve the powers of $(\frac{1}{Q^2})^n; n = 1, 2, 3\ldots$, become important. Therefore, nonperturbative effects are of considerable experimental interest to the oscillation experiments. Furthermore, the higher order perturbative evolution of parton densities is also an important aspect in this kinematic region of x and Q^2, where due to finite value of the strong coupling constant $[\alpha_s(Q^2)]$, terms beyond the leading order (LO) cannot be ignored. In this paper, we have performed the numerical calculations up to next-to-next-to-leading order (NNLO) by using the MMHT nucleonic PDFs parametrization [62]. However, there are many PDFs parametrizations available in the literature for the nucleons like that of MRS [63], MRST [64], GJR [65], CTEQ6.6 [66], MSTW [67], CT10 [68], JR14 [69], CT14 [70], etc. We prefer to use the MMHT PDFs parametrization [62] as it is continuously being updated and supersedes the earlier MRS [63], MRST [64] and MSTW [67] PDFs sets, and it is based on the global analyses of the available hard scattering data like for the pp collision data, deep inelastic scattering data, Drell-Yan data, W and Z production data from LHC, LHCb, ATLAS, and CMS experiments, and the HERA combined ZEUS and H1 data, etc. The MMHT PDFs parametrization [62] dealts independently with the sea quark and antiquark distribution and it is valid in the kinematic range of $10^{-6} \le x \le 1$ and $1 \le Q^2 \le 10^9$ GeV^2. We have observed that the different choices of PDFs parametrization would not make any significant change in the results of nucleon structure functions [71]. In addition to the perturbative evolution of parton densities, we have taken into account the TMC effect following the works of Schienbein *et al.* [72].

Theoretical investigation of nuclear medium effects in the DIS region for x beyond 0.8 is limited in the literature [73–75], especially in the case of neutrino interactions with the nuclear targets. Bodek and Ritchie [76,77] have reported the effect of Fermi motion on the weak nuclear structure functions $F_{iA}^{\rm WI}(x, Q^2)$; $(i = 1$–$3)$ in the region of $x \le 1$ for the different values of Q^2 and Saito *et al.* [73] have studied the effect of Fermi motion on $F_{2A}^{\rm EM}(x, Q^2)$ for $x \ge 1$ at higher values of Q^2 viz. $Q^2 = 100$ GeV^2 by using the various forms for the momentum distribution of nucleons such as ideal Fermi gas type, 2-range Gaussian type, etc., in the different nuclear targets. Frankfurt *et al.* [74] have studied medium effects using the few nucleon correlation model as well as by considering the effect of short range correlations of nucleon on $F_{2A}^{\rm EM}(x, Q^2)$ beyond $x = 1$ and at moderate and high values of Q^2. Furthermore, Fernandez de Cordoba *et al.* [75] have also evaluated the electromagnetic nuclear structure function $F_{2A}^{\rm EM}(x, Q^2)$ for $x \gtrsim 1$ in the local density approximation by considering the effect of nucleon correlations. They obtained the results for carbon, oxygen and iron in the wide range of Q^2 and discussed the importance of DIS to understand the nucleon dynamics in the nuclear medium. One may notice that theoretical investigation of nuclear structure function in the region of low and moderate Q^2 at $x \gtrsim 1$ is lacking particularly for the experiments being performed using the (anti)neutrino beam which motivated us to carry out this study. In the present work, we have theoretically studied the nuclear medium effects in the DIS region for both the electromagnetic and weak interaction channels in the kinematic range of $x \gtrsim 1$, where the effect of Fermi motion and nucleon correlations come into play. These effects have been taken into account through the nucleon spectral function which provides information about energy and momentum distribution of nucleons inside a nucleus, in a microscopic field theoretical model [78,79]. To calculate the spectral function for an interacting Fermi sea in the nuclear medium we have used the nuclear many body theory for infinite nuclear matter and then the local density approximation (LDA) is applied to obtain the results for a finite nucleus. In LDA, nucleon density is calculated at the point of interaction for a volume element d^3r inside the nuclear target and the free lepton-nucleon cross section is folded over the density of the nucleons in the nucleus and integrated over the whole volume of the nucleus. This model has been applied earlier to understand the nuclear medium effects in both the electromagnetic and weak interaction channels up to $x \le 0.8$ [29–32,35,71,80–85], where besides the nucleon-nucleon correlations and Fermi motion some other nuclear medium effects such as shadowing, antishadowing and mesonic cloud contributions are important.

In this work, the numerical results are obtained for the charged lepton and neutrino induced DIS off carbon, argon, iron and lead nuclear targets by incorporating nuclear medium effects like binding energy, Fermi motion and nucleon correlations along with the TMC effect and the PDFs evolution is done at NNLO. In the next section, we present the formalism for $l - A$; $(l = e^{\pm}/\mu^{\pm}, \nu_e/\nu_\mu)$ DIS in brief. In Sec. III, results are presented and discussed which is followed by the summary of this work in Sec. IV.

II. FORMALISM

The general expression of the differential scattering cross section for lepton-nucleus deep inelastic scattering process

$$l^-(k)/\nu_l(k) + A(p_A) \to l^-(k') + X(p'_A); \quad l = e \text{ or } \mu, \tag{2}$$

which is diagrammatically shown in Fig. 2, is given by [29,32]

$$\frac{d^2\sigma_A^{\rm IC}}{dxdy} = \kappa\left[xy^2F_{1A}^{\rm IC}(x,Q^2) + \left(1 - y - \frac{M_N xy}{2E_l}\right)F_{2A}^{\rm IC}(x,Q^2) + xy\left(1-\frac{y}{2}\right)F_{3A}^{\rm IC}(x,Q^2)\right], \tag{3}$$

where in Eq. (2), $k(E_l,\mathbf{k})$ and $k'(E'_l,\mathbf{k}')$ are the four momenta of the incoming and outgoing leptons while $p_A(M_A,\mathbf{0})$ and $p'_A(E'_A,\mathbf{p'_A})$ are the four momenta of the target nucleus and the final state jet of hadrons, respectively. $M_A(=AM_N)$ is the mass of the target nucleus. In Eq. (3), the superscript "IC" stands for the interaction channel which could be either the weak (WI) or electromagnetic (EM) interaction channel with $F_{3A}^{\rm EM}(x,Q^2) = 0$. The constant $\kappa = \frac{8M_N E_l \pi\alpha^2}{Q^4}$ for the EM interaction and $\kappa = \frac{G_F^2 M_N E_l}{\pi}\left(\frac{M_W^2}{M_W^2+Q^2}\right)^2$ for the weak interaction induced processes, α is the strong coupling constant, G_F is Fermi coupling constant, M_W is the mass of W boson, $Q^2(\geq 0)$ is the four momentum transfer square and $y\left(=\frac{p_A\cdot q}{p_A\cdot k} = \frac{E_l - E'_l}{E_l} = \frac{\nu}{E_l}\right)$ is the inelasticity. $F_{iA}^{\rm IC}(x,Q^2)$; $(i = 1\text{–}3)$ are the dimensionless nuclear structure functions. The parity violating nuclear structure function $F_{3A}^{\rm IC}(x,Q^2)$ arises due to the vector–axial vector interference part of the weak interaction and it does not contribute in the case of electromagnetic interaction. To evaluate the nuclear structure functions we perform the numerical calculations in the laboratory frame, where target nucleus is at rest ($p_A^0 = M_A$, $\mathbf{p_A} = 0$). However, the nucleons bound inside the nucleus are not stationary but are moving with a momentum ($p_N \neq 0$) constrained by the Fermi momentum (p_{F_N}) of the nucleon in the nucleus which is given by $p_N \leq p_{F_N}$. In the global Fermi gas model, Fermi momentum of nucleon is taken to be a constant value like $p_{F_N} = 221$ MeV for carbon, $p_{F_N} = 251$ MeV for iron, etc., while in the local density approximation, where the interaction takes place at a point $\mathbf{r}$ lying inside a volume element d^3r, instead of taking a constant density for a given nucleus the lepton scatters from a bound nucleon having density as a function of r, i.e., $\rho_N(r)$ and the corresponding Fermi momentum is given by $p_{F_N} = (3\pi^2\rho_N(r))^{1/3}$. The differential scattering cross section which is evaluated as a function of local density $\rho_N(r)$ is given by

$$d\sigma_A = \int d^3r\rho_N(r)d\sigma_N, \tag{4}$$

where $d\sigma_N$ is the differential cross section of the lepton-nucleon scattering. For a symmetric nuclear matter, each nucleon occupies a volume of $(2\pi\hbar)^3$ and each unit cell is occupied by the two nucleons due to the two possible spin orientations. Hence the number of nucleons in a given volume V are

$$N = 2V\int_0^{p_{F_N}} \frac{d^3p}{(2\pi\hbar)^3} \tag{5}$$

In the natural unit system $\hbar = 1$

$$N = 2V\int_0^{p_{F_N}} \frac{d^3p}{(2\pi)^3}; \text{ or } \rho = \frac{N}{V} = 2\int_0^{p_{F_N}} \frac{d^3p}{(2\pi)^3}n(\mathbf{p},\mathbf{r}), \tag{6}$$

where $n(\mathbf{p},\mathbf{r})$ is the occupation number of a nucleon lying within the Fermi sea with the following constraints

$$n(\mathbf{p},\mathbf{r}) = \begin{cases} 1; \mathbf{p} \leq \mathbf{p_{F_N}} \\ 0; \mathbf{p} > \mathbf{p_{F_N}} \end{cases} \tag{7}$$

Moreover, for a nonsymmetric nucleus such as argon, iron, lead, etc., we have taken into account the different densities for the proton ($\rho_p(r)$) and the neutron ($\rho_n(r)$) which are expressed as

$$\rho_n(r) = \frac{A-Z}{A}\rho(r); \qquad \rho_p(r) = \frac{Z}{A}\rho(r), \tag{8}$$

where $\rho(r)$ is the charged nuclear density and the corresponding Fermi momenta are given by

$$p_{F_n} = (3\pi^2\rho_n(r))^{1/3}; \qquad p_{F_p} = (3\pi^2\rho_p(r))^{1/3} \tag{9}$$

For the nuclear charge density $\rho(r)$ different parametrizations are available in the literature such as harmonic oscillator density, modified harmonic oscillator density, two-parameter Fermi density, three-parameter Fermi density, etc., [86,87]. For the present numerical

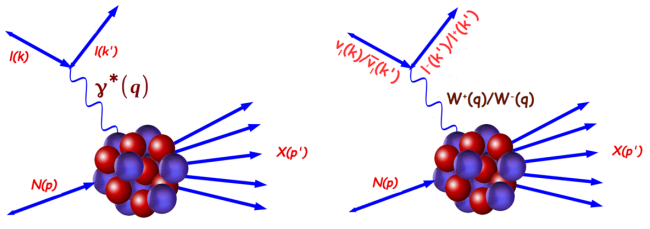

FIG. 2. Feynman diagram showing the deep inelastic scattering processes with bound nucleons for the electromagnetic (left column) and weak (right column) interactions.

TABLE I. Different parameters used for the numerical calculations for various nuclei. For ^{12}C we have used modified harmonic oscillator density(* c_2 is dimensionless) and for ^{40}Ar, ^{56}Fe and ^{208}Pb nuclei, 2-parameter Fermi density have been used, where superscript n and p in density parameters($c_i^{n,p}$; $i = 1, 2$) stand for neutron and proton, respectively. Density parameters for isoscalar and nonisoscalar nuclear targets are given separately in units of fm. The kinetic energy per nucleon(T/A) and the binding energy per nucleon (B.E/A) obtained using Eq. (30) for the different nuclei are given in MeV.

	Nonisoscalar				Isoscalar			
Nucleus	c_1^n	c_1^p	c_2^n	c_2^p	c_1	c_2	B.E./A	T/A
^{12}C	…	…	…	…	1.692	1.082*	7.6	20.0
^{40}Ar	3.64	3.47	0.569	0.569	3.53	0.542	8.6	29.0
^{56}Fe	4.050	3.971	0.5935	0.5935	4.106	0.519	8.8	30.0
^{208}Pb	6.890	6.624	0.549	0.549	6.624	0.549	7.8	32.6

calculations, we have used modified harmonic oscillator (MHO) density for carbon while two-parameter Fermi (2 pF) density for argon, iron and lead which are given by

$$\text{MHO density}: \rho_N(r) = \rho_0\left[1 + c_2\left(\frac{r}{c_1}\right)^2\right],$$
$$\text{2pF density}: \rho_N(r) = \frac{\rho_0}{1 + e^{(r-c_1)/c_2}}$$

with c_1 and c_2 as the density parameters and ρ_0 as the central density [86,87]. These parameters are individually tabulated in Table I for proton and neutron in the case of nonisoscalar nuclear target as well as for nucleon in the case of isoscalar nuclear target.

For a given process the scattering cross section measures the probability of interaction per unit area, i.e.,

$$d\sigma = \Gamma\, dt\, dS, \tag{10}$$

where dS is the differential area, Γ is the decay width of the particle and dt is the time of interaction. Now by using the relations $dt = \frac{dl}{v}$ and $v = \frac{|\mathbf{k}|}{E(\mathbf{k})}$ we relate the integration over time to the integration over space and rewrite the scattering cross section as

$$d\sigma = \Gamma\frac{dt}{dl}\, dS\, dl = \Gamma\frac{1}{v}d^3r, = \Gamma\frac{E(\mathbf{k})}{|\mathbf{k}|}d^3r, \tag{11}$$

where d^3r is the volume element and dl is the length of interaction. The probability of interaction per unit time (Γ) that the incoming lepton will interact with the bound nucleons is related to the lepton self-energy as

$$\Gamma = -\frac{2m_l}{E(\mathbf{k})}\text{Im}\Sigma, \tag{12}$$

using which in Eq. (11), we obtain

$$d\sigma = \frac{-2m_l}{|\mathbf{k}|}\text{Im}\Sigma d^3r, \tag{13}$$

where ImΣ stands for the imaginary part of the neutrino/charged lepton self-energy which is shown in Fig. 3(a). The expression for the neutrino/charged lepton self-energy is obtained by using the Feynman rules and is given by [31]:

$$\Sigma^{\text{IC}}(k) = \kappa\int\frac{d^4q}{(2\pi)^4}\frac{L_{\mu\nu}^{\text{IC}}}{\chi^{\text{IC}}}\frac{1}{(k'^2 - m_l^2 + i\epsilon)}\Pi_{\text{IC}}^{\mu\nu}(q), \tag{14}$$

where $\kappa = \frac{ie^2}{2m_l}(\frac{i2\sqrt{2}G_F}{m_l})$, $\chi = q^4(\frac{(q^2-M_W^2)^2}{M_W^4})$ and $L_{\mu\nu}^{\text{EM}}(L_{\mu\nu}^{\text{WI}})$ is the leptonic tensor for the electromagnetic(weak) interaction process. The expressions for the leptonic tensor are given by

$$L_{\mu\nu}^{\text{EM}} = 8(k_\mu k'_\nu + k_\nu k'_\mu - k.k' g_{\mu\nu});$$
$$L_{\mu\nu}^{\text{WI}} = 8(k_\mu k'_\nu + k_\nu k'_\mu - k.k' g_{\mu\nu} \pm i\epsilon_{\mu\nu\rho\sigma}k^\rho k'^\sigma).$$

$\Pi^{\mu\nu}(q)$ is the intermediate vector boson self-energy which is depicted in Fig. 3(b) and may also be obtained using the similar analogy. By using the Cutkowsky rules one may obtain the imaginary part of the neutrino/charged lepton self-energy for which the detailed formulation has been given in Refs. [30,31].

In the present numerical calculations, we have chosen the momentum transfer along the z–axis, i.e., $q^\mu = (q^0, 0, 0, q^z)$ leading to $x_N = \frac{Q^2}{2p_N\cdot q} = \frac{Q^2}{2(p^0q^0 - p^zq^z)}$. The nucleons bound inside the nucleus interact among

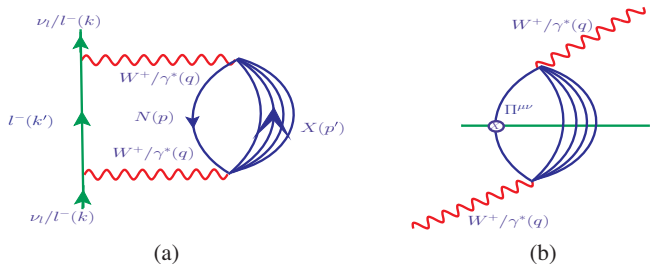

FIG. 3. Feynman diagram representing the (a) neutrino/charged lepton self-energy and (b) intermediate W–boson/virtual photon self-energy.

themselves via the strong interaction. These nucleon-nucleon correlation effects have been taken into account by using the nucleon spectral function calculated in a microscopic field theoretical model [78]. In this field theoretical approach the nucleon propagator which provides information about the propagation of nucleon from initial state to final is written in terms of the hole and particle spectral functions. However, for an inclusive process we need only the hole spectral function and therefore for the present work we will proceed with it. In the literature, some other spectral function models are also available such as given by Vagnoni *et al.* [88] who used the framework of impulse approximation, Megias *et al.* [89] who used superscaling phenomenon, etc. For the numerical calculations of deep inelastic inclusive scattering process, we will use the hole spectral function calculated for the infinite nuclear matter and then the local density approximation is applied to translate these results to finite nuclei.

Let us start with the expression of relativistic free nucleon Dirac propagator $G^0(p^0,\mathbf{p})$ which is written in terms of positive and negative energy states as [30,31]:

$$G^0(p^0,\mathbf{p})=\frac{M_N}{E_N(\mathbf{p})}\left\{\frac{\sum_r u_r(\mathbf{p})\bar{u}_r(\mathbf{p})}{p^0-E_N(\mathbf{p})+i\epsilon}+\frac{\sum_r v_r(-\mathbf{p})\bar{v}_r(-\mathbf{p})}{p^0+E_N(\mathbf{p})-i\epsilon}\right\}, \tag{15}$$

where $u(\mathbf{p})$ and $v(-\mathbf{p})$ are the Dirac spinors satisfying the following identities

$$\sum_r u_r(\mathbf{p})\bar{u}_r(\mathbf{p})=\frac{\not{\mathbf{p}}+M_N}{2M_N};$$
$$\sum_r v_r(-\mathbf{p})\bar{v}_r(-\mathbf{p})=\frac{\not{\mathbf{p}}-M_N}{2M_N}$$

and $E_N(\mathbf{p})=\sqrt{\mathbf{p}^2+M_N^2}$ is the relativistic energy of an on shell nucleon. The nucleon propagator $G^0(p^0,\mathbf{p})$ will retain the positive energy components only as the negative energy components are much suppressed. Hence, by considering only the positive energy component part of Eq. (15), we write the relativistic nucleon propagator in a noninteracting Fermi sea in terms of the occupation number $[n(\mathbf{p})]$ of the nucleons in the Fermi sea as:

$$G^0(p^0,\mathbf{p})=\frac{M_N}{E_N(\mathbf{p})}\sum_r u_r(\mathbf{p})\bar{u}_r(\mathbf{p})\left(\frac{1-n(\mathbf{p})}{p^0-E_N(\mathbf{p})+i\epsilon}+\frac{n(\mathbf{p})}{p^0-E_N(\mathbf{p})-i\epsilon}\right) \tag{16}$$

This representation of nucleon propagator is known as the Lehmann's representation using which the spectral function has been calculated. The terms within the parenthesis in Eq. (16) can be interpreted as follows:

(i) First term corresponds to the particles above the Fermi sea ($\mathbf{p}\geq\mathbf{p_F}$).
(ii) Second term corresponds to the particles below the Fermi sea ($\mathbf{p}<\mathbf{p_F}$).

Inside the Fermi sea, where nucleons interact with each other, the relativistic nucleon propagator is written by using the Dyson series expansion in terms of the nucleon self-energy $\Sigma^N(p)$ as (depicted in Fig. 4):

$$G(p)=G^0(p)+G^0(p)\Sigma^N(p)G^0(p)+G^0(p)\Sigma^N(p)G^0(p)\Sigma^N(p)G^0(p)+\cdots\cdots. \tag{17}$$

In nuclear many body technique, the nucleon self-energy $\Sigma^N(p)$ contains all the information on single nucleon properties. By using Eq. (15) in the above expression, we obtain a geometric progression series:

$$G(p)=\frac{M_N}{E_N(\mathbf{p})}\frac{\sum_r u_r(\mathbf{p})\bar{u}_r(\mathbf{p})}{p^0-E_N(\mathbf{p})+i\epsilon}+\frac{M_N}{E_N(\mathbf{p})}\frac{\sum_r u_r(\mathbf{p})\bar{u}_r(\mathbf{p})}{p^0-E_N(\mathbf{p})+i\epsilon}\Sigma^N(p^0,\mathbf{p})\times\frac{M_N}{E_N(\mathbf{p})}\frac{\sum_r u_r(\mathbf{p})\bar{u}_r(\mathbf{p})}{p^0-E_N(\mathbf{p})+i\epsilon}+\cdots..$$

which on further simplification lead us to the following expression

$$G(p)=\frac{M_N}{E_N(\mathbf{p})}\sum_r\frac{u_r(\mathbf{p})\bar{u}_r(\mathbf{p})}{p^0-E_N(\mathbf{p})-\bar{u}_r(\mathbf{p})\Sigma^N(p^0,\mathbf{p})u_r(\mathbf{p})\frac{M_N}{E_N(\mathbf{p})}} \tag{18}$$

From Eq. (18), it may be noticed that the nucleon self-energy $\Sigma^N(p^0,\mathbf{p})$ absorbs the term $i\epsilon$ in the denominator because $\Sigma^N(p^0,\mathbf{p})$ has a finite imaginary part:

$$\Sigma^N(p^0,\mathbf{p})=\mathrm{Re}\{\Sigma^N(p^0,\mathbf{p})\}+i\mathrm{Im}\{\Sigma^N(p^0,\mathbf{p})\} \tag{19}$$

Real part of the self-energy is related to the effective mass while the imaginary part is related to the lifetime of particles ($\mathrm{Im}\Sigma^N=\frac{1}{\tau}$). Therefore, the expression given in Eq. (18) is modified as

$$G(p)=\frac{M_N}{E_N(\mathbf{p})}\sum_r u_r(\mathbf{p})\bar{u}_r(\mathbf{p})\left[\frac{\{p^0-E_N(\mathbf{p})-\frac{M_N}{E_N(\mathbf{p})}\mathrm{Re}(\Sigma^N)\}+i\{\frac{M_N}{E_N(\mathbf{p})}\mathrm{Im}(\Sigma^N)\}}{\{p^0-E_N(\mathbf{p})-\frac{M_N}{E_N(\mathbf{p})}\mathrm{Re}(\Sigma^N)\}^2+\{\frac{M_N}{E_N(\mathbf{p})}\mathrm{Im}(\Sigma^N)\}^2}\right] \tag{20}$$

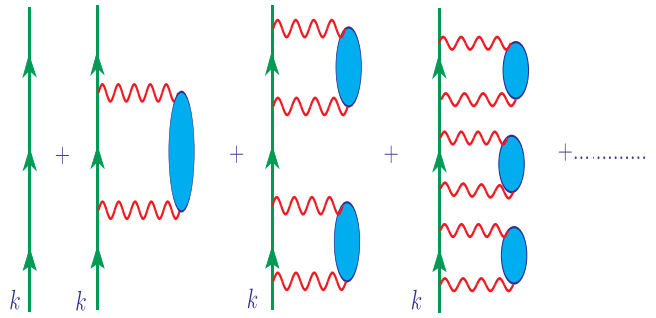

FIG. 4. Diagrammatic representation of nucleon self-energy in the nuclear medium.

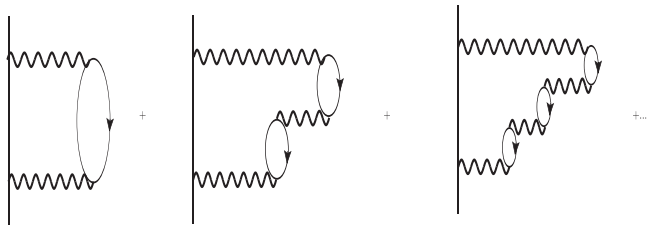

FIG. 5. Diagrammatic representation of the nucleon self-energy including the effects of the medium polarization.

The nucleon propagator $G(p)$ is calculated in terms of the nucleon self-energy $\Sigma^N(p^0,\mathbf{p})$. We have followed a semi-phenomenological approach where the nucleon self-energy uses the input needed for the NN interaction to the NN cross section and for this experimental elastic NN cross section is taken. The nucleon self-energy is written using the techniques of the standard many body theory [90,91]. $G(p)$ is calculated using Eq. (17) by summing over the diagrams shown in Fig. 4, where $\Sigma^0(p^0,\mathbf{p})$ corresponds to Fig. 4(b). The effect of nucleon-nucleon correlations in the calculation of $\Sigma^0(p^0,\mathbf{p})$ is taken into account using the RPA in ladder approximation shown in Fig. 5 which takes into account long range correlations, where the wiggly line represents the NN interaction potential in the one boson exchange model. The NN potential is calculated using π and ρ exchanges to describe the long range part and the Landau-Migdal parameter g' is used to describe the short range part of the potential. The explicit form of the NN potential calculated through the π and ρ exchanges is taken to be

$$V_{si}(q) = (V_L(q)\hat{q}_i\hat{q}_j + V_T(q)(\delta_{ij} - \hat{q}_i\hat{q}_j))\sigma_i\sigma_j\boldsymbol{\tau}\cdot\boldsymbol{\tau}, \quad (21)$$

with V_L and V_T as the longitudinal and transverse part of the spin-isospin interaction and are given by

$$V_L(q) = \frac{f^2}{m_\pi^2}\left(\frac{\mathbf{q}^2}{q_0^2 - \mathbf{q}^2 - m_\pi^2}F_\pi^2(q)C_\pi + g'\right),$$
$$V_T(q) = \frac{f^2}{m_\pi^2}\left(\frac{\mathbf{q}^2}{q_0^2 - \mathbf{q}^2 - m_\rho^2}F_\rho^2(q)C_\rho + g'\right). \quad (22)$$

In the numerical calculations we have used the value of Landau-Migdal parameter $g' = 0.7$, and the values of the parameters $C_\pi = 1$ and $C_\rho = 3.94$. The other parameters in $V(q)$ are taken into account by relating them via meson-NN form factor $F_{\pi/\rho}$ as [91]:

$$F_a(q) = \frac{\Lambda_a^2 - m_a^2}{\Lambda_a^2 - q^2}, \quad (23)$$

where $a = \pi$, ρ and m_a is the meson mass. The value of parameters Λ_π and Λ_ρ are respectively taken to be 1.3 GeV and 1.4 GeV, and $\frac{f^2}{m_\pi^2} = 0.08$. By using the expression of $\Sigma^0(p)$ for nucleon self-energy we obtain its imaginary part, which is quenched specially at low energies and high densities due to the RPA effect. Moreover, it depends on the nucleon energy p^0 as well as nucleon momentum $\mathbf{p}$ in the interacting Fermi sea and fulfills the low-density theorem. The real part of the nucleon self-energy is obtained by means of the dispersion relations using the expressions of the imaginary part. After performing some algebra (see Ref. [30,78] for details), we obtain the following expression for the dressed relativistic nucleon propagator in a nuclear medium in terms of the particle (S_p) and hole (S_h) spectral functions:

$$G(p) = \frac{M_N}{E_N(\mathbf{p})}\sum_r u_r(\mathbf{p})\bar{u}_r(\mathbf{p})\left[\int_{-\infty}^{\mu} d\omega \frac{S_h(\omega,\mathbf{p})}{p^0 - \omega - i\epsilon} + \int_{\mu}^{\infty} d\omega \frac{S_p(\omega,\mathbf{p})}{p^0 - \omega + i\epsilon}\right], \quad (24)$$

where $\omega(= p^0 - M_N)$ is the removal energy and μ is the chemical potential defined in terms of Fermi momentum and the nucleon self-energy (Σ^N) as [91]:

$$\mu = \frac{p_{F_N}^2}{2M_N} + \mathrm{Re}\Sigma^N\left[\frac{p_{F_N}^2}{2M_N}, p_{F_N}\right] \quad (25)$$

The expressions for the hole and particle spectral functions are taken from Ref. [91]:

$$S_h(p^0,\mathbf{p}) = \frac{1}{\pi}\frac{\frac{M_N}{E_N(\mathbf{p})}\mathrm{Im}\Sigma^N(p^0,\mathbf{p})}{(p^0 - E_N(\mathbf{p}) - \frac{M_N}{E_N(\mathbf{p})}\mathrm{Re}\Sigma^N(p^0,\mathbf{p}))^2 + (\frac{M_N}{E_N(\mathbf{p})}\mathrm{Im}\Sigma^N(p^0,\mathbf{p}))^2} \tag{26}$$

when $p^0 \leq \mu$,

$$S_p(p^0,\mathbf{p}) = -\frac{1}{\pi}\frac{\frac{M_N}{E_N(\mathbf{p})}\mathrm{Im}\Sigma^N(p^0,\mathbf{p})}{(p^0 - E_N(\mathbf{p}) - \frac{M_N}{E_N(\mathbf{p})}\mathrm{Re}\Sigma^N(p^0,\mathbf{p}))^2 + (\frac{M_N}{E_N(\mathbf{p})}\mathrm{Im}\Sigma^N(p^0,\mathbf{p}))^2} \tag{27}$$

when $p^0 > \mu$.

In Eq. (24), the term $S_h(\omega,\mathbf{p})d\omega$ represents the joint probability of removing a nucleon from the ground state and $S_p(\omega,\mathbf{p})d\omega$ represents the joint probability of adding a nucleon to the ground state of a nucleus. Hence, one may obtain the spectral function sum rule which is given by

$$\int_{-\infty}^{\mu} S_h(\omega,\mathbf{p})d\omega + \int_{\mu}^{+\infty} S_p(\omega,\mathbf{p})d\omega = 1 \tag{28}$$

We have ensured that the spectral function is properly normalized and checked it by obtaining the correct baryon number (A) for a given nuclear target [30,91]:

$$2\int d^3r \int \frac{d^3p}{(2\pi)^3}\int_{-\infty}^{\mu} d\omega S_h(\omega,\mathbf{p}) = A, \tag{29}$$

where the factor of 2 is a spin factor. The binding energy per nucleon [30,91] for a nucleus is given by

$$|E_A| = -\frac{1}{2}\left(\langle E_N - M_N\rangle + \frac{A-2}{A-1}\langle T\rangle\right) \tag{30}$$

with $\langle T\rangle$ as the average kinetic energy and $\langle E_N\rangle$ as total nucleon energy. In Ref. [29,30], we have discussed that for an inclusive scattering process only the hole spectral function (S_h) is required and the nuclear hadronic tensor ($W_A^{\mu\nu}$) is expressed in terms of the nucleon hole spectral function and the nucleonic hadronic tensor ($W^{\mu\nu}$) for an isoscalar nuclear target as

$$W_A^{\mu\nu} = 4\int d^3r \int \frac{d^3p}{(2\pi)^3}\frac{M_N}{E_N(\mathbf{p})} \times \int_{-\infty}^{\mu} dp^0 S_h(p^0,\mathbf{p},\rho(r))W^{\mu\nu}(p,q), \tag{31}$$

where the factor of 4 is for spin-isospin of the nucleon. However, for a nonisoscalar nuclear target $W_A^{\mu\nu}$ is written in terms of the proton/neutron hole spectral function (S_h^j; $j = p,\ n$) and the corresponding hadronic tensor ($W_j^{\mu\nu}$; $j = p,\ n$) as

$$W_A^{\mu\nu} = 2\sum_{j=p,n}\int d^3r \int \frac{d^3p}{(2\pi)^3}\frac{M_N}{E_N(\mathbf{p})} \times \int_{-\infty}^{\mu_j} dp^0 S_h^j(p^0,\mathbf{p},\rho_j(r))W_j^{\mu\nu}(p,q), \tag{32}$$

where the factor of 2 is due to the two possible projections of nucleon spin, μ_j; ($j = p,\ n$) is the chemical potential for the proton/neutron and ρ_j is the density which is incorporated in an appropriate manner for proton/neutron individually. The density parameters for proton and neutron corresponding to the different nuclear targets have been given in Table I. The isoscalarity corrections should be appropriately accounted for as most of the lepton scattering experiments are being performed using the heavy nuclear targets, where neutron excess becomes significant. In LDA, the spectral functions of protons and neutrons which are the function of their local Fermi momenta are normalized as:

$$2\int \frac{d^3p}{(2\pi)^3}\int_{-\infty}^{\mu} d\omega S_h^{p,n}(\omega,p,p_{F_{p,n}}(\mathbf{r})) = \rho_{p,n}(\mathbf{r}), \tag{33}$$

leading to the following normalization for $S_h^{p,n}$:

$$2\int d^3r \int \frac{d^3p}{(2\pi)^3}\int_{-\infty}^{\mu_p} S_h^p(\omega,\mathbf{p},\rho_p(r))\ d\omega = Z, \tag{34}$$

$$2\int d^3r \int \frac{d^3p}{(2\pi)^3}\int_{-\infty}^{\mu_n} S_h^n(\omega,\mathbf{p},\rho_n(r))\ d\omega = N. \tag{35}$$

It is important to point out that hole spectral function for proton (S_h^p) is the function of proton density [$\rho_p(r)$] and thus the proton's Fermi momentum ($p_{F_p}(r) = (3\pi^2\rho_p(r))^{1/3}$), while S_h^n depends on the neutron density [$\rho_n(r)$] and the corresponding Fermi momentum for neutron ($p_{F_n} = (3\pi^2\rho_n(r))^{1/3}$).

Now, by using Eq. (32), we take the appropriate components of the nucleon ($W_N^{\mu\nu}$) and the nuclear ($W_A^{\mu\nu}$) hadronic tensors along the x, y and z axes, and obtain the following expressions of dimensionless nuclear structure functions for a nonisoscalar nuclear target [29,30,32]:

$$F_{1A}^{\rm IC}(x_A,Q^2)=2\sum_{j=p,n}AM_N\int d^3r\int\frac{d^3p}{(2\pi)^3}\frac{M_N}{E_N(\mathbf{p})}\int_{-\infty}^{\mu_j}dp^0S_h^j(p^0,\mathbf{p},\rho_j(r))\left[\frac{F_{1j}^{\rm IC}(x_N,Q^2)}{M_N}+\left(\frac{p^x}{M_N}\right)^2\frac{F_{2j}^{\rm IC}(x_N,Q^2)}{\nu_N}\right], \quad (36)$$

$$F_{2A}^{\rm IC}(x_A,Q^2)=2\sum_{j=p,n}\int d^3r\int\frac{d^3p}{(2\pi)^3}\frac{M_N}{E_N(\mathbf{p})}\int_{-\infty}^{\mu_j}dp^0S_h^j(p^0,\mathbf{p},\rho_j(r))\times\left(\frac{M_N}{p^0-p^z\gamma}\right)\times F_{2j}^{\rm IC}(x_N,Q^2)$$
$$\times\left[\left(\frac{Q}{q^z}\right)^2\left(\frac{|\mathbf{p}|^2-(p^z)^2}{2M_N^2}\right)+\frac{(p^0-p^z\gamma)^2}{M_N^2}\left(\frac{p^zQ^2}{(p^0-p^z\gamma)q^0q^z}+1\right)^2\right], \quad (37)$$

$$F_{3A}^{\rm IC}(x_A,Q^2)=2A\sum_{j=p,n}\int d^3r\int\frac{d^3p}{(2\pi)^3}\frac{M_N}{E_N(\mathbf{p})}\int_{-\infty}^{\mu_j}dp^0S_h^j(p^0,\mathbf{p},\rho_j(r))\times\frac{q^0}{q^z}\left(\frac{p^0q^z-p^zq^0}{p\cdot q}\right)F_{3j}^{\rm IC}(x_N,Q^2), \quad (38)$$

where $\nu_N=\frac{p\cdot q}{M_N}=\frac{p^0q^0-p^zq^z}{M_N}$ and $\gamma=\frac{q^z}{q^0}$. For an isoscalar nuclear target ($F_{iA}=\frac{F_{iA}^p+F_{iA}^n}{2}$) the factor of 2 in the above expressions [Eqs. (36)–(38)] is replaced by 4 and μ_j is replaced by μ [see Eqs. (25) and (31)].

In the limit of $Q^2\to\infty$, $\nu\to\infty$ with $x\to$ finite, the nucleon structure functions become the function of dimensionless Bjorken variable x only, i.e., $F_{ij}^{\rm IC}(x_N)$; $(j=p,\ n)$ and are expressed in terms of the parton distribution functions (PDFs) at the leading order (LO) as

$$F_{2j}^{\rm EM}(x)=\sum_i e_i^2x\{q_i(x)+\bar{q}_i(x)\};$$
$$F_{2j}^{\rm WI}(x)=\sum_i x\{q_i(x)+\bar{q}_i(x)\};$$
$$xF_{3j}^{\rm WI}(x)=\sum_i x\{q_i(x)-\bar{q}_i(x)\}, \quad (39)$$

where index i runs over the flavor of quarks, e_i is the charge of corresponding quark or antiquark and $xq_i(x)/x\bar{q}_i(x)$ is the probability of finding a quark/antiquark inside the nucleon carrying a momentum fraction x of the momentum of the target nucleon. For the free nucleon case, Callan-Gross relation has been used to obtain $F_{1j}^{\rm IC}(x)$ in terms of PDFs at the leading order, i.e., $F_{2j}^{\rm IC}(x)=2xF_{1j}^{\rm IC}(x)$. For $Q^2\to\infty$, the strong coupling constant ($\alpha_s(Q^2)$) is small and the terms beyond the leading order are negligible, but at the finite values of Q^2, the strong coupling constant is large and the higher order terms like the next-to-leading order (NLO), next-to-next-to-leading order (NNLO), etc., cannot be ignored. Hence, the dimensionless nucleon structure functions are written as a perturbative series expansion of the strong coupling constant [92,93] as

$$F_{iN}(x,Q^2)=\left(\frac{\alpha_s(Q^2)}{4\pi}\right)^0F_{iN}^{LO}(x,Q^2)+\left(\frac{\alpha_s(Q^2)}{4\pi}\right)^1F_{iN}^{\rm NLO}(x,Q^2)+\left(\frac{\alpha_s(Q^2)}{4\pi}\right)^2F_{iN}^{\rm NNLO}(x,Q^2)+\cdots \quad (40)$$

In the present work, we have performed the evolution of PDFs up to next-to-next-to-the leading order (NNLO) and use the MMHT nucleonic PDFs parametrization [62] for the numerical calculations. Furthermore, at low and moderate values of Q^2 the nonperturbative effect of target mass corrections (TMC) comes into play which is important at high x. We have incorporated the TMC effect following the operator product expansion approach [72]. The target mass corrected nucleon structure functions are given by [29,72]

$$F_{1N}^{\rm TMC}(x,Q^2)=F_{1N}(\xi)\left(\frac{x}{\xi\lambda}\right)(1+2\varrho(1-\xi)^2),$$
$$F_{2N}^{\rm TMC}(x,Q^2)=F_{2N}(\xi)\left(\frac{x^2}{\xi^2\lambda^3}\right)(1+6\varrho(1-\xi)^2),$$
$$F_{3N}^{\rm TMC}(x,Q^2)=F_{3N}(\xi)\left(\frac{x}{\xi\lambda^2}\right)(1-\varrho(1-\xi)ln\xi),$$

where $\varrho=\frac{M_N^2x\xi}{Q^2\lambda}$, $\lambda=\sqrt{1+\frac{4M_N^2x^2}{Q^2}}$ and the Nachtmann variable $\xi=\frac{2x}{1+\lambda}$. Following the present formalism, we have obtained the results of the nuclear structure functions which are required to evaluate the results of the differential scattering cross sections. These numerical calculations are performed in the kinematic region of high $x(\gtrsim 0.8)$ and moderate Q^2 ($\leq$20 GeV^2) as depicted in Fig. 1 and the results are presented in Figs. 6–11.

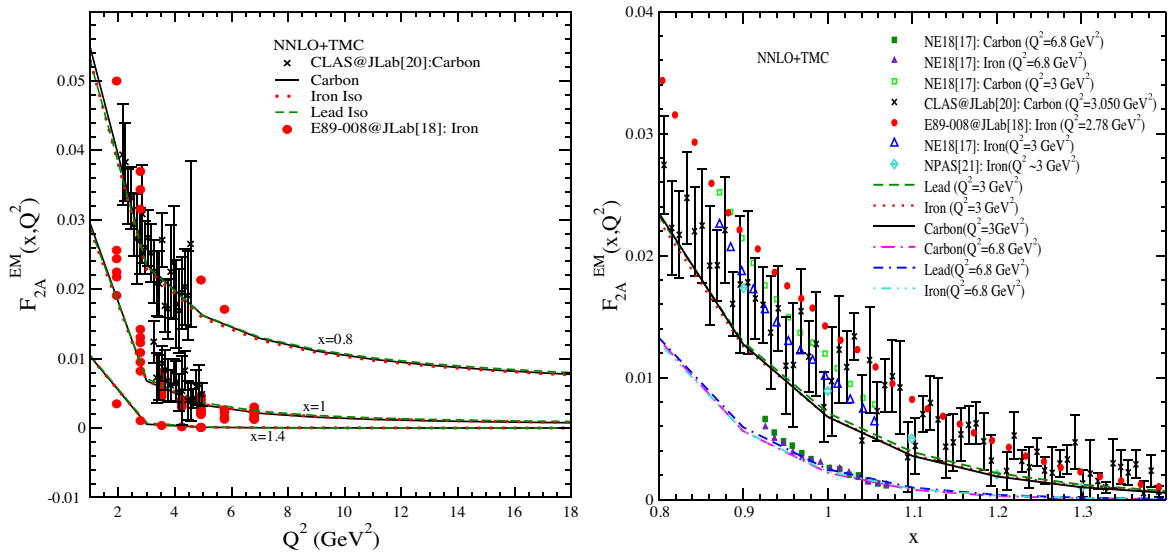

FIG. 6. Results of electromagnetic nuclear structure function. Left panel: $F_{2A}^{\mathrm{EM}}(x,Q^2)$ vs Q^2 at different values of x and Right panel: $F_{2A}^{\mathrm{EM}}(x,Q^2)$ vs x at $Q^2 = 3$ and 6.8 GeV^2 are shown for carbon, iron and lead. These results are obtained at NNLO incorporating the TMC effect but without applying any cut on the center of mass energy W and are compared with the experimental data of inclusive $e^- - {}^{56}$Fe scattering from NE18 experiment at NPAS [17], E89-008 experiment at JLab [18], experiment at NPAS [21] as well as with the experimental data for $e^- - {}^{12}$C from NE18 experiment at NPAS [17] and CLAS Hall B experiment at JLab [20]. The theoretical curves are the results only for the DIS region while the experimental results are for the inclusive process.

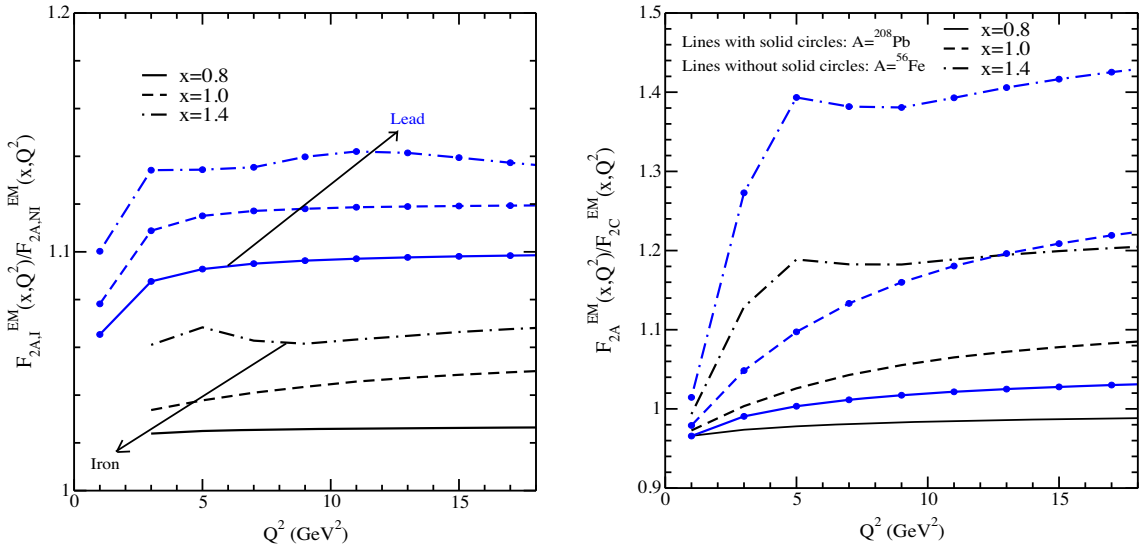

FIG. 7. Results for the ratios of electromagnetic nuclear structure functions for isoscalar to nonisoscalar nuclear target viz. $\frac{F_{2A,I}^{\mathrm{EM}}(x,Q^2)}{F_{2A,\mathrm{NI}}^{\mathrm{EM}}(x,Q^2)}$; (I $\equiv$ isoscalar, NI $\equiv$ nonisoscalar) (left panel) and $\frac{F_{2A}^{\mathrm{EM}}(x,Q^2)}{F_{2C}^{\mathrm{EM}}(x,Q^2)}$ (isoscalar nuclear targets: right panel) are shown for iron and lead vs Q^2 at the different values of x. "A" represents the same nuclear target both in the numerator and denominator. These results have been obtained using nucleonic PDFs at NNLO with TMC effect.

III. RESULTS AND DISCUSSION

In this section, we present the results of the electromagnetic and weak nuclear structure functions using Eqs. (36)–(38) as well as the differential cross sections using Eq. (3) relevant to the kinematic region of the charged lepton-nucleus scattering experiments such as CLAS, NE18, etc., and neutrino-nucleus scattering experiments like MINERvA and DUNE. All the numerical results are obtained for the deep inelastic scattering by incorporating the nuclear medium effects like the binding energy, Fermi motion and nucleon correlations through the use of hole spectral function. Theoretical results are obtained for the

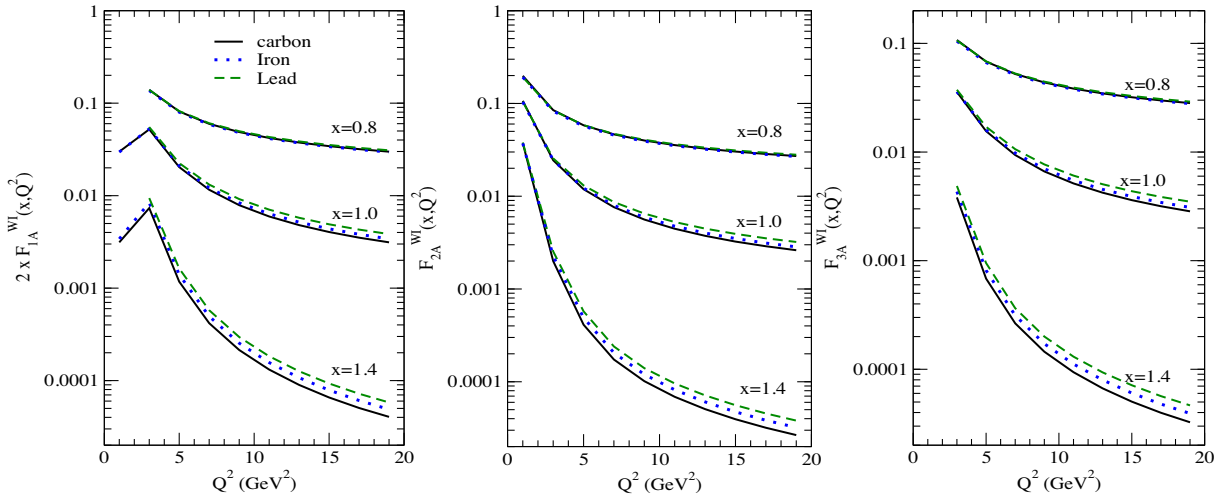

FIG. 8. Results of weak nuclear structure functions $F_{iA}^{\mathrm{WI}}(x, Q^2)$; $(i = 1\text{–}3)$ vs Q^2 at the different values of x are shown for carbon, iron and lead. These results are obtained without applying any cut on the center of mass energy W at NNLO incorporating the TMC effect. Iron and lead are treated as isoscalar nuclear targets.

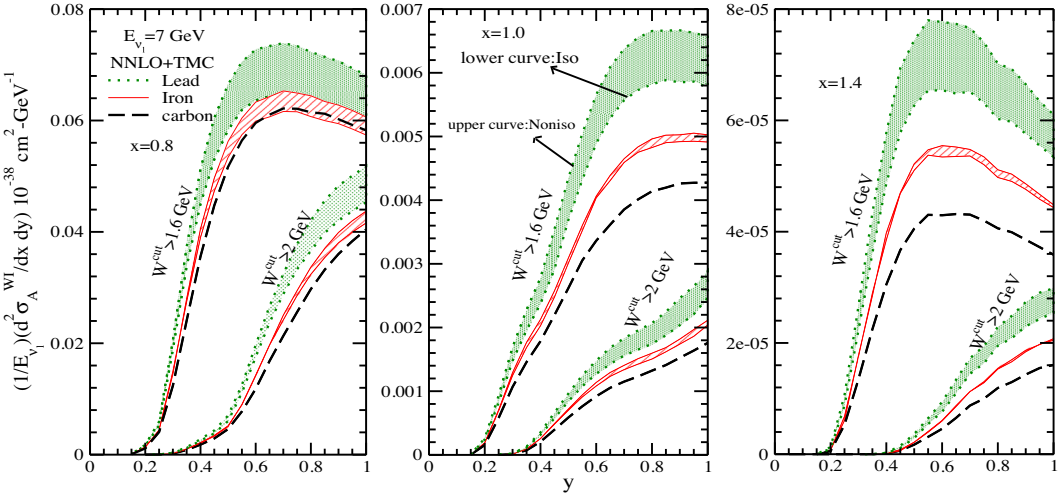

FIG. 9. Results of $\frac{1}{E_{\nu_l}}\frac{d^2\sigma_A^{\mathrm{WI}}}{dxdy}$ vs y for $\nu_\mu - A$; $(A = {}^{12}\mathrm{C}, {}^{56}\mathrm{Fe}, {}^{208}\mathrm{Pb})$ DIS are shown at NNLO with TMC effect. These results are obtained for $E_{\nu_l} = 7$ GeV by applying the cuts of 1.6 GeV and 2.0 GeV on the CM energy, treating iron and lead isoscalar as well as nonisoscalar nuclear targets.

carbon, hydrocarbon, argon, iron and lead nuclear targets in the region of $x \gtrsim 0.8$ keeping $Q^2 \geq 1$ GeV^2 without and with a cut on the center of mass energy W. Furthermore, in argon, iron and lead, isoscalarity corrections are also included wherever mentioned.

In the left panel of Fig. 6, the results of the electromagnetic nuclear structure function $F_{2A}^{\mathrm{EM}}(x, Q^2)$ vs Q^2 for the nuclear targets $A = {}^{12}\mathrm{C}, {}^{56}\mathrm{Fe}, {}^{208}\mathrm{Pb}$ are shown at the different values of x viz. $x = 0.8$, 1.0 and 1.4. For the numerical calculations iron and lead are treated as isoscalar nuclear targets [Eq. (31)]. In this kinematic region the contribution from the deep inelastic channel to the total cross section of inclusive electron-nucleus scattering process is expected to be small as compared to the contributions from the inelastic resonance production and quasielastic scattering processes. Nevertheless, the contribution from the deep inelastic region as may be observed from the figure is significant. With the increase in x, $F_{2A}^{\mathrm{EM}}(x, Q^2)$ decreases and thus the contribution of DIS to the cross section becomes gradually small. The numerical results for $F_{2A}^{\mathrm{EM}}(x, Q^2)$ are compared with the available experimental data for the inclusive electron-nucleus scattering [18,20] in the region of moderate Q^2 ($\leq$7 GeV^2). In the right panel of the figure, the results are presented for $F_{2A}^{\mathrm{EM}}(x, Q^2)$ vs x at the two different values of Q^2 viz. $Q^2 = 3$ GeV^2 and $Q^2 = 6.8$ GeV^2 in carbon, iron and lead nuclear targets. It may be observed that due to the Q^2 variation, there is significant difference in the results of nuclear structure

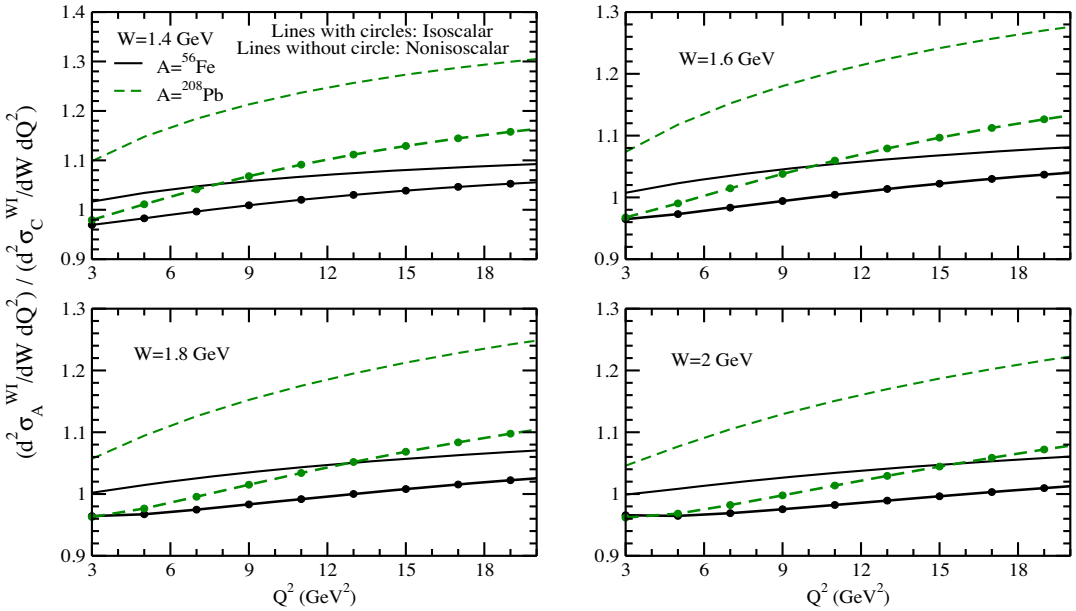

FIG. 10. Results for the ratio of $(\frac{d^2\sigma_A^{\rm WI}}{dWdQ^2})/(\frac{d^2\sigma_C^{\rm WI}}{dWdQ^2})$; $(A = {}^{56}\text{Fe}, {}^{208}\text{Pb})$ vs Q^2 for $\nu_\mu - A$ DIS are shown at NNLO with TMC effect. Nuclear targets iron and lead are treated to be isoscalar as well as nonisoscalar. Lines without solid circles represent the results for the nonisoscalar nuclei while lines with solid circles represent the results obtained for the isoscalar nuclear targets. Solid lines correspond to iron and dashed lines correspond to lead.

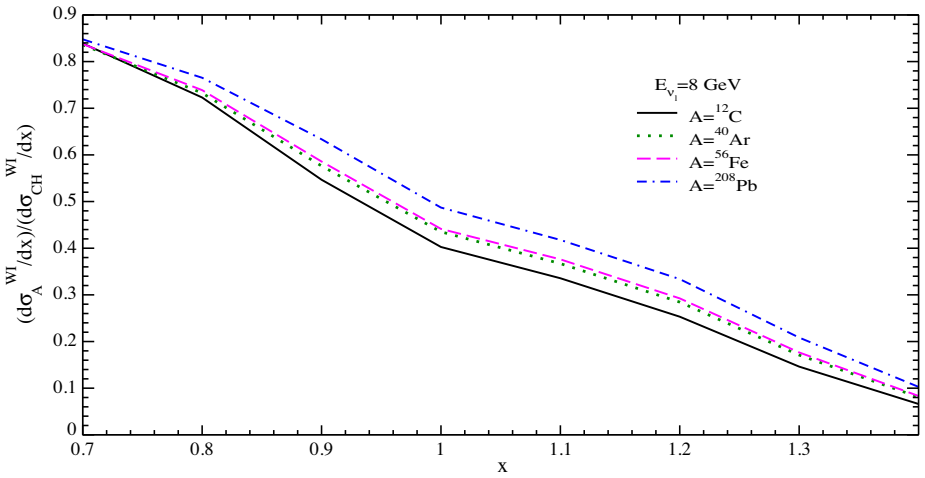

FIG. 11. Results for the ratio of $(\frac{d\sigma_A^{\rm WI}}{dx})/(\frac{d\sigma_{\rm CH}^{\rm WI}}{dx})$; $(A = {}^{12}\text{C}, {}^{40}\text{Ar}, {}^{56}\text{Fe}, {}^{208}\text{Pb})$ vs x for $\nu_\mu - A$ DIS are shown at $E_{\nu_l} = 8$ GeV keeping $Q^2 > 1$ GeV^2 and $W^{\rm cut} > 2$ GeV at NNLO with TMC effect. Nuclear targets argon, iron and lead are treated to be isoscalar.

function $F_{2A}^{\rm EM}(x, Q^2)$, however, this difference becomes small with the increase in x. These results are also compared with the inclusive electron-nucleus scattering experimental data available for carbon [17,20] and iron [17,18,21]. One may notice that our theoretical results obtained using the present formalism for the DIS process underestimates the experimental data. It may be because of the missing contributions from the quasielastic and resonance production processes which we have not taken into account. Hence in order to understand the experimental results for the inclusive electron-nucleus scattering process, a theoretical study for the Q^2 dependence of the inelastic resonance production and quasielastic processes should also be performed which is a topic of separate study.

For the heavy nuclear targets like iron $({}^{56}_{26}\text{Fe}, N > Z)$ and lead $({}^{208}_{82}\text{Pb}, N \gg Z)$ which have different neutron and proton numbers, isoscalarity corrections become important. Hence, it is required to observe the effect of the corrections arising due to neutron excess on nuclear structure functions for a given nuclear target by treating it to be isoscalar $(N = Z)$ as well as nonisoscalar $(N \neq Z)$. In our theoretical

model as discussed in Sec. II for a nonisoscalar nuclear target, the hole spectral function is separately normalized to the proton [Eq. (34)] and neutron [Eq. (35)] numbers while for an isoscalar nuclear target S_h is normalized to the nucleon numbers [Eq. (29)].

To explicitly study the isoscalarity corrections we have obtained the results for the ratio $\frac{F^{\rm EM}_{2A,\rm I}(x,Q^2)}{F^{\rm EM}_{2A,\rm NI}(x,Q^2)}$; (I $\equiv$ isoscalar, NI $\equiv$ nonisoscalar) vs Q^2 at a fixed value of x. These results are presented in the left panel of Fig. 7. One may notice that the ratios viz. $\frac{F^{\rm EM}_{2\rm Fe,I}(x,Q^2)}{F^{\rm EM}_{2\rm Fe,NI}(x,Q^2)}$ and $\frac{F^{\rm EM}_{2\rm Pb,I}(x,Q^2)}{F^{\rm EM}_{2\rm Pb,NI}(x,Q^2)}$ have significant deviation from unity which highlights the importance of nonisoscalarity, especially in the heavier nuclear target like ^{208}Pb. For example, in lead ($N \gg Z$) this nonisoscalarity effect is about 9%–10% in the entire range of Q^2 at $x = 0.8$, while for $x = 1.4$, this difference increases to 13%–14%. Whereas for a nonisoscalar nuclear target such as iron, where $N \gtrsim Z$ this effect is small like 2%–3% at $x = 0.8$ and 6%–7% at $x = 1.4$. Except for low values of $Q^2 \leq 7$ GeV^2, this ratio is found to be almost Q^2 independent. Furthermore, to observe the nuclear medium modifications of $F^{\rm EM}_{2A}(x, Q^2)$ in different nuclear targets the results for the ratios of iron to carbon $(\frac{F^{\rm EM}_{2\rm Fe}(x,Q^2)}{F^{\rm EM}_{2C}(x,Q^2)})$ and lead to carbon $(\frac{F^{\rm EM}_{2\rm Pb}(x,Q^2)}{F^{\rm EM}_{2C}(x,Q^2)})$ have been obtained treating all the nuclear targets viz. ^{12}C, ^{56}Fe and ^{208}Pb to be isoscalar. These results are shown in the right panel of the Fig. 7. From the figure, one may observe that the nuclear medium effects become more pronounced with the increase in mass number A, Bjorken x as well as four momentum transfer square Q^2. Quantitatively, the increase in the nuclear medium effects in lead vs carbon is of about ∼5%, 16% and 20% at $Q^2 = 3$ GeV^2, $Q^2 = 9$ GeV^2 and $Q^2 = 15$ GeV^2, respectively when x is kept fixed say here at $x = 1.0$. With the increase in x, say at $x = 1.4$ this difference becomes 27%, 38%, and 42% for the respective values of Q^2 mentioned above. In our earlier works on the study of nuclear medium effects in the DIS region [29,30,32] for x lying in the range of $0 \leq x \leq 0.8$, we found that the nuclear medium effect gradually decreases with the increase in Q^2. Present results show that the effects of the isoscalarity corrections and the nuclear medium modifications are significant even at $x \gtrsim 1$.

In Fig. 8, the numerical results for the weak nuclear structure functions $2xF^{\rm WI}_{1A}(x, Q^2)$, $F^{\rm WI}_{2A}(x, Q^2)$, and $F^{\rm WI}_{3A}(x, Q^2)$ are presented. It may be noticed that all the three nuclear structure functions decrease in magnitude with the increase in x and Q^2. We have also looked into the validity of Callan-Gross relation, i.e., $F_{2N}(x) = 2xF_{1N}(x)$, by comparing the results of $2xF^{\rm WI}_{1A}(x, Q^2)$ and $F^{\rm WI}_{2A}(x, Q^2)$ in the presence of nuclear medium effects which have been discussed earlier in the case of electromagnetic nuclear structure functions in Ref. [30,32] for $x < 0.8$. CG relation holds good at the leading order for the free nucleon target, however, it shows deviation at low and moderate values of Q^2 when gluonic contributions become significant beyond the leading order. In the present kinematic region of x and Q^2, we find that there is significant deviation of the ratio $\frac{F_{2A}(x,Q^2)}{2xF_{1A}(x,Q^2)}$ from unity (not shown here explicitly), for example, at $Q^2 = 3$ GeV^2 this deviation in the ratio $\frac{F^{\rm WI}_{2A}(x,Q^2)}{2xF^{\rm WI}_{1A}(x,Q^2)}$ is ∼40% at $x = 0.8$, 52% at $x = 1.0$ and 72% at $x = 1.4$ which is almost independent of the nucleon mass number A. Whereas, at larger values of Q^2 viz. $Q^2 =$ 15 GeV^2 this deviation decreases to 12%, 20% and 40% at $x = 0.8$, $x = 1.0$ and $x = 1.4$, respectively. The deviation of the ratio $\frac{F_{2A}(x,Q^2)}{2xF_{1A}(x,Q^2)}$ from unity becomes more pronounced with the increase in x and decrease in Q^2.

Using the results of weak nuclear structure functions $F^{\rm WI}_{iA}(x, Q^2)$; $i = 1$–3, we have obtained the results for $\nu_\mu - A$ double differential scattering cross sections $\frac{1}{E_{\nu_l}}\frac{d^2\sigma^{\rm WI}_A}{dxdy}$; ($A = {}^{12}$C, ^{56}Fe, ^{208}Pb) vs y [using Eq. (3)], and the ratio of differential cross section for iron to carbon and lead to carbon, i.e., $(\frac{d^2\sigma_A}{dWdQ^2})/(\frac{d^2\sigma_C}{dWdQ^2})$; ($A = {}^{56}$Fe, ^{208}Pb) vs Q^2 by treating iron and lead both as an isoscalar as well as nonisoscalar nuclear targets. These results are shown in Figs. 9 and 10, respectively. In these results the effect of the center of mass energy cut on the differential scattering cross sections is also discussed. The significance of CM energy cut in the region of $x \leq 0.8$ have already been discussed by us in Refs. [29,32,35,57,71] and by the other theoretical groups [49,52,94–96], but for $x \gtrsim 1$ no study is available in the weak sector.

In Fig. 9, the numerical results of $\frac{1}{E_{\nu_l}}\frac{d^2\sigma^{\rm WI}_A}{dxdy}$; ($A = {}^{12}$C, ^{56}Fe, ^{208}Pb) vs y, are presented at $E_{\nu_l} = 7$ GeV with the kinematical cuts of $W^{\rm cut} > 1.6$ GeV (upper ones) and $W^{\rm cut} > 2$ GeV (lower ones). The numerical results for carbon are shown by the long dashed lines while the results for iron and lead are shown by the bands filled with the diagonal line pattern and the shaded pattern, respectively. The upper curve in the band is the results when a given nuclear target is treated to be nonisoscalar while the lower curve of the band is the result when nuclear target is treated as isoscalar. Hence, by using these bands one may easily quantify the nonisoscalarity effect. We have found that the enhancement in the results due to the nonisoscalarity effect is 14–15% at $x = 0.8$ and $y = 0.4$–0.6 in lead and it increases to 18–19% at $x = 1.4$. It may be observed that the isoscalarity effect is not independent of x and we find that it is also Q^2 dependent. We have also observed the effect of $W^{\rm cut}$ on the differential scattering cross section by comparing the results corresponding to $W^{\rm cut} > 1.6$ GeV and $W^{\rm cut} > 2$ GeV. We have found that when a cut of $W^{\rm cut} > 2$ GeV is applied, the results of the differential cross section for $\nu_\mu - {}^{56}$Fe get reduced by about 75% at $x = 0.8$–1.0 and $y = 0.6$ as compared to the results

obtained with $W^{\rm cut} > 1.6$ GeV. However, for $y = 0.8$ this reduction becomes 46% at $x = 0.8$ and 68% at $x = 1.0$. It shows that the effect of $W^{\rm cut}$ is quite significant in the present kinematic region of x.

Since it is important to understand both the effects of CM energy W as well as Q^2 on the differential scattering cross sections, we have also performed the numerical calculations to observe the effect of Q^2 variation when W is kept fixed. These results would be important to explicitly investigate the behavior of differential cross section in different regions of CM energy cut corresponding to the second resonance region up to the region of deep inelastic scattering.

In Fig. 10, the results for the ratios of the double differential scattering cross section, $(\frac{d^2\sigma_A^{\rm WI}}{dWdQ^2})/(\frac{d^2\sigma_C^{\rm WI}}{dWdQ^2})$; $(A = {}^{56}{\rm Fe}, {}^{208}{\rm Pb})$ vs Q^2 are presented at fixed values of the center of mass energy. These results are obtained keeping the ongoing experimental analysis of MINERvA collaboration in mind for $\nu_\mu/\bar{\nu}_\mu$–nucleus scattering in the region of $x \gtrsim 1$ [38]. It may be noticed from the figure that the nuclear medium effects become more pronounced for the heavier nuclear targets at all values of W. For example, the increase in the nuclear medium effects in the ratio $(\frac{d^2\sigma_{\rm Fe}^{\rm WI}}{dWdQ^2})/(\frac{d^2\sigma_C^{\rm WI}}{dWdQ^2})$ obtained for $W = 1.4$ GeV is about 3% at $Q^2 = 3$ GeV^2 and ∼6% at $Q^2 = 20$ GeV^2. Whereas, in lead this ratio $(\frac{d^2\sigma_{\rm Pb}^{\rm WI}}{dWdQ^2})/(\frac{d^2\sigma_C^{\rm WI}}{dWdQ^2})$ increase to about 17% at $Q^2 = 20$ GeV^2. However, when the numerical calculations are performed at $W = 2$ GeV, the effect of nuclear medium modifications becomes small, for example, it is found to be 2% in $(\frac{d^2\sigma_{\rm Fe}^{\rm WI}}{dWdQ^2})/(\frac{d^2\sigma_C^{\rm WI}}{dWdQ^2})$ and 8% in $(\frac{d^2\sigma_{\rm Pb}^{\rm WI}}{dWdQ^2})/(\frac{d^2\sigma_C^{\rm WI}}{dWdQ^2})$ at $Q^2 = 20$ GeV^2. It shows that at higher values of Q^2 the nuclear medium modifications have a weak dependence on A. Furthermore, we have obtained these ratios by treating the nuclear targets to be nonisoscalar and the results are shown by the lines without solid circles. By comparing the results for the isoscalar vs nonisoscalar nuclear targets, it may be observed that the nonisoscalarity effect is significant in the entire region of Q^2, however, the nonisoscalarity effect in these ratios of cross section decreases with the increase in CM energy cut, for example, at $Q^2 = 3$ GeV^2 there is an enhancement (from isoscalarity) of about ∼12% at $W = 1.4$ GeV and 8% at $W = 2$ GeV. While at $Q^2 = 20$ GeV^2 this enhancement in the ratio is found to be 14% irrespective of CM energy W. It shows that in the region of high Q^2 the nonisoscalarity effect becomes almost independent of W considered in this work.

In the short baseline neutrino experiments such as ICARUS [39,40] and SBND [41,42] as well as in the long baseline neutrino experiment DUNE [44–46], liquid argon (^{40}Ar) is being used as nuclear target for the cross section measurements in the energy region of GeVs. However, the fixed target neutrino-nucleus scattering experiment MINERvA [23,25] is using hydrocarbon (CH), water (H_2O), iron (^{56}Fe) and lead (^{208}Pb) nuclear targets and have recently reported the results showing the x-dependence of the inclusive cross section ratios, i.e., $\frac{d\sigma_A/dx}{d\sigma_{\rm CH}/dx}$ vs x in the neutrino energy range of $2 \leq E_{\nu_l} \leq 20$ GeV [23]. In Fig. 11, we have explicitly shown the x–dependence of the nuclear medium effects for the deep inelastic scattering cross section ratios $(\frac{d\sigma_A^{\rm WI}}{dx})/(\frac{d\sigma_{\rm CH}^{\rm WI}}{dx})$; $(A = {}^{12}{\rm C}, {}^{40}{\rm Ar}, {}^{56}{\rm Fe}, {}^{208}{\rm Pb})$ at the neutrino energy $E_{\nu_l} = 8$ GeV. These results are obtained with the kinematic constraints of $Q^2 > 1$ GeV^2 and $W^{\rm cut} > 2$ GeV treating argon, iron and lead to be isoscalar nuclear targets. It is important to point out that the ratio of lead to hydrocarbon $(\frac{d\sigma_{\rm Pb}/dx}{d\sigma_{\rm CH}/dx})$ is higher than the ratios $\frac{d\sigma_{\rm Fe}/dx}{d\sigma_{\rm CH}/dx}$, $\frac{d\sigma_{\rm Ar}/dx}{d\sigma_{\rm CH}/dx}$ and $\frac{d\sigma_{\rm C}/dx}{d\sigma_{\rm CH}/dx}$ as the Fermi motion effect is more pronounced in the heavier nuclear targets. For a meaningful comparison with the MINERvA's experimental results [23], a separate study of x–dependence of the nuclear medium effects in quasielastic and inelastic resonance production processes is also needed. This work is in progress and will be reported elsewhere. The theoretical predictions for argon would be relevant for the understanding of experimental results from DUNE [44–46].

IV. SUMMARY AND CONCLUSIONS

In this paper, the results of electromagnetic and weak nuclear structure functions have been presented along with the results of the differential scattering cross sections for the weak interaction induced $\nu_\mu - A$ deep inelastic scattering in the kinematic region of high Bjorken $0.8 \leq x \leq 1.4$. These results are obtained at NNLO with the TMC effect, for carbon, hydrocarbon, argon, iron and lead. This study provides an overview of the nuclear medium modifications of the nucleon structure functions and the differential cross sections for the DIS process in the region of $x \gtrsim 1$ which has not been much explored yet. Our findings are summarized as:

(i) A comparison of the numerical results for $F_{2A}^{\rm EM}(x, Q^2)$ with the inclusive electron-nucleus scattering experimental data for the electromagnetic nuclear structure function [17,18,20,21] imply that for $x \gtrsim 1$, there is significant contribution from the deep inelastic scattering region.

(ii) Kinematic boundaries for the transition regions are needed to be precisely defined to distinguish between the resonance and DIS regions in order to avoid the double counting for the measurements of the neutrino-nucleus scattering cross sections. We find that when a CM energy cut of $W^{\rm cut} > 2$ GeV vs $W^{\rm cut} > 1.6$ GeV is used to evaluate the $\nu_\mu - {}^{12}$C differential cross sections, then there is reduction in the DIS cross section which is more pronounced in the region of low and intermediate y, like for $x = 0.8$

this reduction is 80% at $y = 0.6$ and 52% at $y = 0.8$. The reduction in the cross section with $W^{\rm cut}$ in the DIS region clearly shows that to determine the relative contributions of the inelastic resonance excitations and the DIS to the differential cross sections, especially in the region of low and intermediate y, proper kinematic constrains are required to be well understood.

(iii) The effect of CM energy cut in the evaluation of cross section has also x dependence, like at a fixed value of y say, $y = 0.6$, the differential cross section for $W^{\rm cut} > 2$ GeV vs $W^{\rm cut} > 1.6$ GeV gets reduced by 80% at $x = 0.8$ and 90% at $x = 1.4$ in ^{12}C.

(iv) Isoscalarity corrections becomes more pronounced with the increase in x and $(N - Z)/A$.

(v) Theoretical predictions for $F_{iA}^{\rm WI}(x, Q^2)$; $(i = 1\text{–}3)$, $\frac{d^2\sigma_A^{\rm WI}}{dxdy}$, $(\frac{d^2\sigma_A^{\rm WI}}{dWdQ^2})/(\frac{d^2\sigma_C^{\rm WI}}{dWdQ^2})$ and $(\frac{d\sigma_A^{\rm WI}}{dx})/(\frac{d\sigma_{\rm CH}^{\rm WI}}{dx})$ presented in this work would be helpful in understanding the upcoming experimental results from the MINERvA collaboration and the planned DUNE experiment.

ACKNOWLEDGMENTS

F. Z. is thankful to the Council of Scientific & Industrial Research (CSIR), India, for providing the research associate fellowship with award letter No. 09/112(0622)2K19 EMR-I. M. S. A. is thankful to the Department of Science and Technology (DST), Government of India for providing financial assistance under Grant No. SR/MF/PS-01/2016-AMU/G.

[1] J. J. Aubert *et al.* (European Muon Collaboration), Phys. Lett. **123B**, 275 (1983).
[2] J. Gomez, R. G. Arnold, P. E. Bosted, C. C. Chang, A. T. Katramatou *et al.*, Phys. Rev. D **49**, 4348 (1994).
[3] P. Amaudruz *et al.* (New Muon Collaboration), Nucl. Phys. **B441**, 3 (1995).
[4] M. Arneodo *et al.* (New Muon Collaboration), Nucl. Phys. **B441**, 12 (1995).
[5] K. Ackerstaff *et al.* (HERMES Collaboration), Phys. Lett. B **475**, 386 (2000); **567**, 339(E) (2003).
[6] A. C. Benvenuti *et al.* (BCDMS Collaboration), Phys. Lett. B **189**, 483 (1987).
[7] G. Bari *et al.* (BCDMS Collaboration), Phys. Lett. **163B**, 282 (1985).
[8] J. Seely *et al.*, Phys. Rev. Lett. **103**, 202301 (2009).
[9] E. P. Segarra, T. Ježo, A. Accardi, P. Duwentäster, O. Hen, T. J. Hobbs, C. Keppel, M. Klasen, K. Kovařík, and A. Kusina *et al.*, Phys. Rev. D **103**, 114015 (2021).
[10] A. J. Freese, W. Cosyn, and M. M. Sargsian, Phys. Rev. D **99**, 114019 (2019).
[11] K. J. Eskola, P. Paakkinen, H. Paukkunen, and C. A. Salgado, arXiv:2112.12462.
[12] R. Abdul Khalek, J. J. Ethier, and J. Rojo (NNPDF Collaboration), Acta Phys. Polon. Supp. **12**, 927 (2019).
[13] H. Khanpour and S. Atashbar Tehrani, Phys. Rev. D **93**, 014026 (2016).
[14] M. Hirai, S. Kumano, and T. H. Nagai, Phys. Rev. C **76**, 065207 (2007).
[15] D. de Florian, R. Sassot, P. Zurita, and M. Stratmann, Phys. Rev. D **85**, 074028 (2012).
[16] J. Arrington, J. Bane, A. Daniel, N. Fomin, D. Gaskell, J. Seely, R. Asaturyan, F. Benmokhtar, W. Boeglin, P. Bosted *et al.*, Phys. Rev. C **104**, 065203 (2021).
[17] J. Arrington, P. Anthony, R. G. Arnold, E. J. Beise, J. E. Belz *et al.*, Phys. Rev. C **53**, 2248 (1996).
[18] J. Arrington, C. S. Armstrong, T. Averett, O. K. Baker, L. de Bever *et al.*, Phys. Rev. C **64**, 014602 (2001).
[19] M. Osipenko *et al.* (CLAS Collaboration), Phys. Rev. C **73**, 045205 (2006).
[20] M. Osipenko *et al.* (CLAS Collaboration), Nucl. Phys. **A845**, 1 (2010).
[21] B. W. Filippone, R. D. McKeown, R. G. Milner, D. H. Potterveld, D. B. Day *et al.*, Phys. Rev. C **45**, 1582 (1992).
[22] A. C. Benvenuti *et al.* (BCDMS Collaboration), Z. Phys. C **63**, 29 (1994).
[23] B. G. Tice *et al.* (MINERνA Collaboration), Phys. Rev. Lett. **112**, 231801 (2014).
[24] M. Vakili *et al.* (CCFR Collaboration), Phys. Rev. D **61**, 052003 (2000).
[25] J. Mousseau *et al.* (MINERνA Collaboration), Phys. Rev. D **93**, 071101 (2016).
[26] A. Bodek and U. K. Yang, Nucl. Phys. B, Proc. Suppl. **112**, 70 (2002).
[27] I. C. Cloet, W. Bentz, and A. W. Thomas, Phys. Lett. B **642**, 210 (2006).
[28] C. Andreopoulos *et al.*, Nucl. Instrum. Methods Phys. Res., Sect. A **614**, 87 (2010).
[29] F. Zaidi, H. Haider, M. Sajjad Athar, S. K. Singh, and I. Ruiz Simo, Phys. Rev. D **101**, 033001 (2020).
[30] H. Haider, F. Zaidi, M. Sajjad Athar, S. K. Singh, and I. Ruiz Simo, Nucl. Phys. **A943**, 58 (2015).
[31] H. Haider, F. Zaidi, M. Sajjad Athar, S. K. Singh, and I. Ruiz Simo, Nucl. Phys. **A955**, 58 (2016).
[32] F. Zaidi, H. Haider, M. Sajjad Athar, S. K. Singh, and I. Ruiz Simo, Phys. Rev. D **99**, 093011 (2019).
[33] D. Ruterbories *et al.* (MINERνA Collaboration), Phys. Rev. D **104**, 092007 (2021).

[34] A. Filkins *et al.* (MINERνA Collaboration), Phys. Rev. D **101**, 112007 (2020).
[35] F. Zaidi, V. Ansari, M. S. Athar, H. Haider, I. R. Simo, and S. K. Singh, Phys. Rev. D **105**, 033010 (2022).
[36] K. Kovarik, A. Kusina, T. Jezo, D. B. Clark, C. Keppel, F. Lyonnet, J. G. Morfin, F. I. Olness, J. F. Owens, I. Schienbein *et al.*, Phys. Rev. D **93**, 085037 (2016).
[37] I. Schienbein, J. Y. Yu, C. Keppel, J. G. Morfin, F. Olness, and J. F. Owens, Phys. Rev. D **77**, 054013 (2008).
[38] Daniel Ruterbories (private communication).
[39] F. Tortorici *et al.* (ICARUS Collaboration), Nucl. Part. Phys. Proc. **306–308**, 154 (2019).
[40] P. A. Machado, O. Palamara, and D. W. Schmitz, Annu. Rev. Nucl. Part. Sci. **69**, 363 (2019).
[41] M. Antonello *et al.* (MicroBooNE, LAr1-ND, and ICARUS-WA104 Collaborations), arXiv:1503.01520.
[42] R. Acciarri *et al.* (SBND Collaboration), J. Instrum. **15**, P06033 (2020).
[43] P. Abratenko *et al.* (MicroBooNE Collaboration), Phys. Rev. Lett. **128**, 151801 (2022).
[44] B. Abi *et al.* (DUNE Collaboration), arXiv:1807.10334.
[45] B. Abi *et al.* (DUNE Collaboration), J. Instrum. **15**, P12004 (2020).
[46] B. Abi *et al.* (DUNE Collaboration), Eur. Phys. J. C **80**, 978 (2020).
[47] C. Anderson *et al.* (ArgoNeuT Collaboration), Phys. Rev. Lett. **108**, 161802 (2012).
[48] R. Acciarri *et al.* (ArgoNeuT Collaboration), Phys. Rev. D **89**, 112003 (2014).
[49] S. Kretzer and M. H. Reno, Phys. Rev. D **66**, 113007 (2002).
[50] E. A. Paschos and J. Y. Yu, Phys. Rev. D **65**, 033002 (2002).
[51] Y. S. Jeong and M. H. Reno, Phys. Rev. D **82**, 033010 (2010).
[52] K. Hagiwara, K. Mawatari, and H. Yokoya, Nucl. Phys. **B668**, 364 (2003); **B701**, 405(E) (2004).
[53] Y. Hayato, Acta Phys. Pol. B **40**, 2477 (2009).
[54] C. Andreopoulos *et al.* (NuSTEC Collaboration), arXiv:1907.13252.
[55] L. Alvarez-Ruso, A. M. Ankowski, M. Sajjad Athar, C. Bronner, L. Cremonesi, K. Duffy, S. Dytman, A. Friedland, A. P. Furmanski, K. Gallmeister *et al.*, arXiv:2009.04285.
[56] L. A. Ruso, A. M. Ankowski, S. Bacca, A. B. Balantekin, J. Carlson, S. Gardiner, R. González-Jiménez, R. Gupta, T. J. Hobbs, M. Hoferichter *et al.*, arXiv:2203.09030.
[57] M. Sajjad Athar and J. G. Morfin, J. Phys. G **48**, 034001 (2021).
[58] M. Tzanov *et al.* (NuTeV Collaboration), Phys. Rev. D **74**, 012008 (2006).
[59] J. P. Berge *et al.*, Z. Phys. C **49**, 187 (1991).
[60] E. Oltman *et al.*, Z. Phys. C **53**, 51 (1992).
[61] G. Onengut *et al.* (CHORUS Collaboration), Phys. Lett. B **632**, 65 (2006).
[62] L. A. Harland-Lang, A. D. Martin, P. Motylinski, and R. S. Thorne, Eur. Phys. J. C **75**, 204 (2015).
[63] A. D. Martin, R. G. Roberts, and W. J. Stirling, Phys. Rev. D **37**, 1161 (1988).
[64] A. D. Martin, R. G. Roberts, W. J. Stirling, and R. S. Thorne, Eur. Phys. J. C **23**, 73 (2002).
[65] M. Glück, P. Jimenez-Delgado, and E. Reya, Eur. Phys. J. C **53**, 355 (2008).
[66] P. M. Nadolsky, H. L. Lai, Q. H. Cao, J. Huston, J. Pumplin, D. Stump, W. K. Tung, and C. P. Yuan, Phys. Rev. D **78**, 013004 (2008).
[67] A. D. Martin, W. J. Stirling, R. S. Thorne, and G. Watt, Eur. Phys. J. C **63**, 189 (2009).
[68] S. Dulat, T.-J. Hou, J. Gao, J. Huston, P. Nadolsky, J. Pumplin, C. Schmidt, D. Stump, and C.-P. Yuan, Phys. Rev. D **89**, 113002 (2014).
[69] P. Jimenez-Delgado and E. Reya, Phys. Rev. D **89**, 074049 (2014).
[70] S. Dulat, T.-J. Hou, J. Gao, M. Guzzi, J. Huston, P. Nadolsky, J. Pumplin, C. Schmidt, D. Stump, and C.-P. Yuan, Phys. Rev. D **93**, 033006 (2016).
[71] M. Sajjad Athar and S. K. Singh, *The Physics of Neutrino Interactions* (Cambridge University Press, Cambridge, England, 2020), 10.1017/9781108489065.
[72] I. Schienbein *et al.*, J. Phys. G **35**, 053101 (2008).
[73] K. Saito and T. Uchiyama, Z. Phys. A **322**, 299 (1985).
[74] L. L. Frankfurt and M. I. Strikman, Phys. Rep. **160**, 235 (1988).
[75] P. Fernandez de Cordoba, E. Marco, H. Muther, E. Oset, and A. Faessler, Nucl. Phys. **A611**, 514 (1996).
[76] A. Bodek and J. L. Ritchie, Phys. Rev. D **24**, 1400 (1981).
[77] A. Bodek and J. L. Ritchie, Phys. Rev. D **23**, 1070 (1981).
[78] E. Marco, E. Oset, and P. Fernández de Córdoba, Nucl. Phys. **A611**, 484 (1996).
[79] L. L. Frankfurt and M. I. Strikman, Phys. Lett. B **183**, 254 (1987).
[80] M. Sajjad Athar, S. K. Singh, and M. J. Vicente Vacas, Phys. Lett. B **668**, 133 (2008).
[81] M. Sajjad Athar, I. Ruiz Simo, and M. J. Vicente Vacas, Nucl. Phys. **A857**, 29 (2011).
[82] H. Haider, I. R. Simo, M. Sajjad Athar, and M. J. V. Vacas, Phys. Rev. C **84**, 054610 (2011).
[83] H. Haider, I. Ruiz Simo, and M. Sajjad Athar, Phys. Rev. C **85**, 055201 (2012).
[84] H. Haider, I. R. Simo, and M. Sajjad Athar, Phys. Rev. C **87**, 035502 (2013).
[85] H. Haider, M. Sajjad Athar, S. K. Singh, and I. R. Simo, J. Phys. G **44**, 045111 (2017).
[86] C. W. De Jager, H. De Vries, and C. De Vries, At. Data Nucl. Data Tables **14**, 479 (1974); H. De Vries, C. W. De Jager, and C. De Vries, At. Data Nucl. Data Tables **36**, 495 (1987).
[87] C. Garcia-Recio, J. Nieves, and E. Oset, Nucl. Phys. **A547**, 473 (1992).
[88] E. Vagnoni, O. Benhar, and D. Meloni, Phys. Rev. Lett. **118**, 142502 (2017).
[89] G. D. Megias, J. E. Amaro, M. B. Barbaro, J. A. Caballero, and T. W. Donnelly, Phys. Rev. D **94**, 013012 (2016).
[90] Claude Itzykson and Jean-Bernard Zuber, *Quantum Field Theory*, 4th ed. (McGraw Hill Publication, Singapore, 1988), ISBN: 0-07-Y66353-X.

[91] P. Fernandez de Cordoba and E. Oset, Phys. Rev. C **46**, 1697 (1992).
[92] W. L. van Neerven and A. Vogt, Nucl. Phys. **B568**, 263 (2000).
[93] W. L. van Neerven and A. Vogt, Nucl. Phys. **B588**, 345 (2000).
[94] K. M. Graczyk, AIP Conf. Proc. **1222**, 238 (2010).
[95] O. Lalakulich, W. Melnitchouk, and E. A. Paschos, Phys. Rev. C **75**, 015202 (2007).
[96] A. Gazizov, M. Kowalski, K. S. Kuzmin, V. A. Naumov, and C. Spiering, EPJ Web Conf. **116**, 08003 (2016).